International Journal of Coal Geology 259 (2022) 104030

Contents lists available at ScienceDirect

International Journal of Coal Geology

journal homepage: www.elsevier.com/locate/coal

Hydrothermal activity in ultra-deep strata and its geological significance for deep earth gas exploration: Implications from pyrobitumen in the Ediacaran-lower Cambrian Strata, Sichuan Basin

Lianqiang Zhu [a,b], Guangdi Liu [a,b,*], Zezhang Song [a,b,*], Zhang Benjian [c], Wenzhi Zhao [a,b], Xingwang Tian [c], Kui Ma [c], Yunlong Wang [c], Dailin Yang [c], Qiang Li [a,b], Chao Gen [c], Jiaxun Lu [c]

[a] State Key Laboratory of Petroleum Resources and Prospecting, China University of Petroleum, Beijing 102249, PR China
[b] College of Geosciences, China University of Petroleum, Beijing 102249, PR China
[c] Southwest Oil and Gas Field Company PetroChina, Chengdu 610041, PR China

ARTICLE INFO

Keywords:
Optical texture
Pyrobitumen
Hydrothermal activity
Crude oil cracking
Central Sichuan Basin

ABSTRACT

Abundant pyrobitumen related to an abnormal thermal event has been observed in the Ediacaran-lower Cambrian reservoirs of the central Sichuan Basin. Using reflected light microscopy, this study classified reservoir pyrobitumen in the Ediacaran-lower Cambrian into three groups: isotropic, mosaic, and fibrous; the mosaic pyrobitumen was further subdivided into fine-grained, medium-grained, and coarse-grained. Based on organic elemental analysis, carbon isotopic composition, nuclear magnetic resonance, X-ray diffraction, thermogravimetric-mass spectrometry, and fluid inclusion geochemistry, the relationship between the optical texture of pyrobitumen and hydrothermal temperature was determined and the influence of hydrothermal activity on crude oil cracking is discussed. With the exception of the mosaic pyrobitumen (quinoline insoluble matter-enriched tar pad precursor) found in the most porous reservoir zone, the optical texture in the Ediacaran-lower Cambrian reservoirs can be used to trace the hydrothermal activity, which occurred at the end of the Permian and may be related to the Emeishan mantle plume. The hydrothermal fluid may have invaded the strata of the second and fourth members of the Dengying Formation and the Longwangmiao Formation, along deep faults in the Gaoshiti area and migrated laterally to the northeast. The intrusion of the hydrothermal fluid directly promoted the cracking of crude oil in the reservoirs, and this behavior advances the previously accepted cracking time by approximately 60 Ma. The study found that hydrothermal activity promoted the cracking of crude oil in the Ediacaran-lower Cambrian reservoirs, which is a significant recognition for understanding the history of hydrocarbon accumulation in the Sichuan Basin.

1. Introduction

Solid bitumen is usually generated from the thermal cracking, gas deasphalting, and biodegradation of crude oil in source rocks or reservoirs (Tissot and Welte, 1984; Hunt, 1996; Waples, 2000). Commonly, solid bitumen with high reflectivity and maturity (bitumen reflectance > 0.7%) is called pyrobitumen; it evolves from solid bitumen with low maturity, and is characterized by a minor extractable fraction (Goodarzi and Stasiuk, 1991; Landis and Castaño, 1995).

Low-maturity solid bitumen is isotropic; in contrast, high-maturity pyrobitumen can exhibit both optical isotropy and anisotropy. According to the size of the anisotropic regions, anisotropic pyrobitumen can be divided into five categories: fine-grain mosaic (FM), medium-grain mosaic (MM), coarse-grain mosaic (CM), domain, and fibrous pyrobitumens (Patrick et al., 1973; Sanada, 1978; Grint et al., 1979; White and Price, 1974). The optical textures of pyrobitumens were first recognized in coking coal and then artificially generated from the pyrolysis of oil and solid bitumen (Taylor, 1961; Brooks and Taylor, 1965; White, 1976; Marsh, 1973; Hatshorme, 1974). The molecular orientation and chemical composition of pyrobitumen are the primary factors controlling optical anisotropy, and both of them are altered through the pyrolysis process (the increase in maturity) (White, 1976; Mochida et al., 1980; Forrest and Marsh, 1981). In addition, the softening point, C/H atomic ratio, polycyclic aromatic hydrocarbon content, and graphitization

* Corresponding authors at: State Key Laboratory of Petroleum Resources and Prospecting, China University of Petroleum, Beijing 102249, PR China.
E-mail addresses: lgd@cup.edu.cn (G. Liu), songzz@cup.edu.cn (Z. Song).

https://doi.org/10.1016/j.coal.2022.104030
Received 25 November 2021; Received in revised form 20 May 2022; Accepted 20 May 2022
Available online 25 May 2022

degree are all positively correlated with the maturity of solid bitumen (Jacob, 1989; Landis and Castaño, 1995; Tian et al., 2013).

Research on coking coal helps explain the generation of anisotropic pyrobitumen. At a specific pressure, as the heating treatment proceeds, the small aromatic molecules in the isotropic bitumen are condensed into large plane lamella molecules and layered into spherical intermediate building units. Then, the intermediate building units are directly stacked into mesophase spheres. Finally, the mesophase spheres fuse to form anisotropic pyrobitumen (Brooks and Taylor, 1965; Heidenreich et al., 1968; Ban and Hess, 1971, 1976; Yamada et al., 1974; Li and Wang, 2005; Li et al., 2005). Petroleum coke studies have shown that the optical texture of pyrobitumen depends on the properties of the precursor and the heating conditions (Marsh and Cornford, 1976; White, 1976). Temperature is an essential factor affecting the optical texture of pyrobitumen (Marsh and Cornford, 1976; White, 1976; Yokono et al., 1986; Fathollahi et al., 2005; Eksilioglu et al., 2006). Owing to the thermal stability of aromatic hydrocarbons, the temperature of the thermal polycondensation reaction ranges from 350 to 500 °C (Yokono et al., 1986; Fathollahi et al., 2005; Eksilioglu et al., 2006). The mesophase spheres cannot be generated when the temperature is lower than 300 °C, resulting in isotropic pyrobitumen (Yokono et al., 1986; Shen, 2003; Fathollahi et al., 2005; Eksilioglu et al., 2006; Sun et al., 2020). When the temperature exceeds 300 °C, the mesophase spheres can gradually grow and fuse to form anisotropic pyrobitumen (Brooks and Taylor, 1965; Heidenreich et al., 1968; Ban and Hess, 1971, 1976; Yamada et al., 1974; Li and Wang, 2005; Li et al., 2005). Under normal circumstances, with an increase in temperature, the optical texture of pyrobitumen shows a regular transition from isotropic → FM → MM → CM → fibrous (Stasiuk, 1997; White and Price, 1974). However, NSO compounds and quinoline insoluble matter (QI) in the pyrobitumen precursor can significantly affect the optical texture. An enrichment of NSO compounds and QI will significantly inhibit the fusion of the mesophase spheres and lead to only one kind of product— mosaic pyrobitumen. Furthermore, when the O concentration exceeds 7%, mesophase spheres cannot be formed (Taylor, 1961; Taylor et al., 1993; Figueiras et al., 1998; Gong et al., 2001; Liu et al., 2003a,b; Xu et al., 2002). In addition, factors such as pressure and reaction circumstance will also affect the optical texture of pyrobitumen (Goodarzi, 1985; Fathollahi et al., 2005; Wang et al., 2008; Cheng and Wang, 2009). However, temperature and chemical composition remain the controlling factors for the optical properties of pyrobitumen.

As the degree of thermal maturity increases, the optical texture of pyrobitumen shows similar changes under experimental and natural conditions. In recent years, abundant reservoir pyrobitumens have been discovered in deep gas fields (e.g., Anyue gas field) in the central Sichuan Basin and are widely distributed in the Ediacaran-Lower Cambrian reservoirs (burial depth > 4500 m) (Wang et al., 2013; Wu et al., 2013; Yang et al., 2018; Gao et al., 2017; Song et al., 2021). These pyrobitumens show differential optical textures-optical isotropy and anisotropy, with mosaic and fibrous textures occuring in the anisotropic pyrobitumen. In most studies, the co-existence of isotropic and anisotropic pyrobitumen in the reservoir suggests an unusual thermal history, such as a magmatic or hydrothermal intrusion (Goodarzi, 1993; Wilson, 2000; Rimmer et al., 2015). Previous studies on vitrinite reflectance and maturity parameters in these reservoirs in the central Sichuan Basin suggest that the generation of the anisotropic pyrobitumen is associated with hydrothermal activity (Wang et al., 2013; Wu et al., 2013; Yang et al., 2016; Gao et al., 2017). As an important thermal event in the Sichuan Basin, the Emeishan mantle plume, which generated hydrothermal activity in the region, is thought to be related to the formation of these anisotropic pyrobitumen (Boven et al., 2002; Yuan et al., 2014; Zhang et al., 2008; Zhang et al., 2013; Yang et al., 2018; Gao et al., 2017).

The natural gas and pyrobitumen in the Ediacaran-Lower Cambrian are derived from the crude oil cracking in the paleo-oil reservoirs (Zhu et al., 2015; Gao et al., 2017; Shi et al., 2017; Zhang, 2019). As products of crude oil cracking, the origins of the pyrobitumen and natural gas in the Ediacaran-Lower Cambrian reservoirs were closely related (Zheng et al., 2014; Wei et al., 2015a; Luo et al., 2015a, 2015b, 2015c). Because the pyrobitumen is of hydrothermal origin, the generation of the natural gas in these reservoirs may be related to hydrothermal activity. However, to date, few scholars have linked the generation of natural gas to hydrothermal activity. Most studies suggest that natural gas in the Ediacaran-Lower Cambrian reservoirs in the central Sichuan Basin was derived from the normal cracking of crude oil. The influence of hydrothermal activity on the formation of ultra-deep gas reservoirs in the central Sichuan Basin is still unknown.

Reservoir pyrobitumen carries geochemical information, which can be used for research on hydrocarbon accumulation mechanisms in ultra-deep strata. Crude oil cracking is usually completed before 200 °C (Pang, 2010; Sun et al., 2013). The highest temperature in the Ediacaran-Lower Cambrian reservoirs was near 200 °C and the crude oil was thought to be cracked into highly matured pyrobitumen and natural gas at this temperature (Xu et al., 2014; Wei et al., 2015a; Zhu et al., 2015; Zhu et al., 2022). Natural gas is primarily a dry gas composed of CH_4, carrying little valuable geochemical information, which severely restricts the in-depth study of ultra-deep natural gas accumulation and evolution (Connan et al., 1995; Manzano et al., 1997; Mankiewicz et al., 2009; Cai et al., 2013). In addition, pyrobitumen in the Ediacaran-Lower Cambrian reservoirs is another end product of crude oil cracking (Zou et al., 2014; Luo et al., 2015a, 2015b, 2015c; Xie et al., 2021). Its occurrence state, optical properties, organic elemental composition, carbon isotopic composition, and internal structure record various geological and geochemical processes that occurred after crude oil was generated; thus, the geological information contained in the pyrobitumen plays an extremely important role in the study of ultra-deep gas reservoirs (Tian et al., 2013; Holman et al., 2014; Gao et al., 2018; Shi et al., 2017).

The optical anisotropy of pyrobitumen is closely related to thermal anomalies (Khavari-Khorosani and Murchison, 1978; Goodarzi and Stasiuk, 1991; Goodarzi, 1993; Gize, 1986). To the authors' knowledge, no study has established the relationship between the optical texture of natural pyrobitumen and hydrothermal temperature. Based on organic elements, carbon isotopes, nuclear magnetic resonance (NMR), X-ray diffraction (XRD), thermogravimetric (TG)-mass spectrometry and fluid inclusion geochemistry, this study established this relationship. Then, the hydrothermal fluid migration was traced based on the spatial distribution of the pyrobitumen. Finally, by integrating the analysis of the period and behavior of hydrothermal activity and gas inclusions captured by hydrothermal minerals, the hydrothermal influence to the gas accumulation and evolution processes of the Ediacaran-Lower Cambrian gas reservoirs in the central Sichuan Basin was examined. This study provided a novel method for reconstructing the evolution process of these reservoirs.

2. Geological setting

The Ediacaran-Lower Cambrian reservoirs are the frontiers for ultra-deep natural gas exploration in the Sichuan Basin. In recent years, the Anyue Ediacaran-Lower Cambrian giant gas field had been discovered in the central Sichuan Basin; its main natural gas producing strata are the Dengying (DY) and the Longwangmiao (LWM) formations (Du et al., 2014; Xu et al., 2014; Wei et al., 2015a; Zhu et al., 2015). The DY Formation consists of carbonate deposited in a marginal platform facies, dominated by algal dolomite; it can be divided into four members from bottom to top, namely the D-1, D-2, D-3, and D-4 members, respectively (Yang et al., 2018; Zhou et al., 2017; Feng et al., 2021). Being affected by the Tongwan tectonic movement, the D-2 and D-4 are characterized by well-developed dissolution space, making them the main gas-producing units in the DY Formation (Luo et al., 2015a, 2015b, 2015c; Shan et al., 2016; Jin et al., 2016; Hu et al., 2020) (Fig. 1). The LWM Formation is a carbonate stratum deposited in gentle sloping platform facies. The pore space occurs primarily in granular dolomite, with well-developed

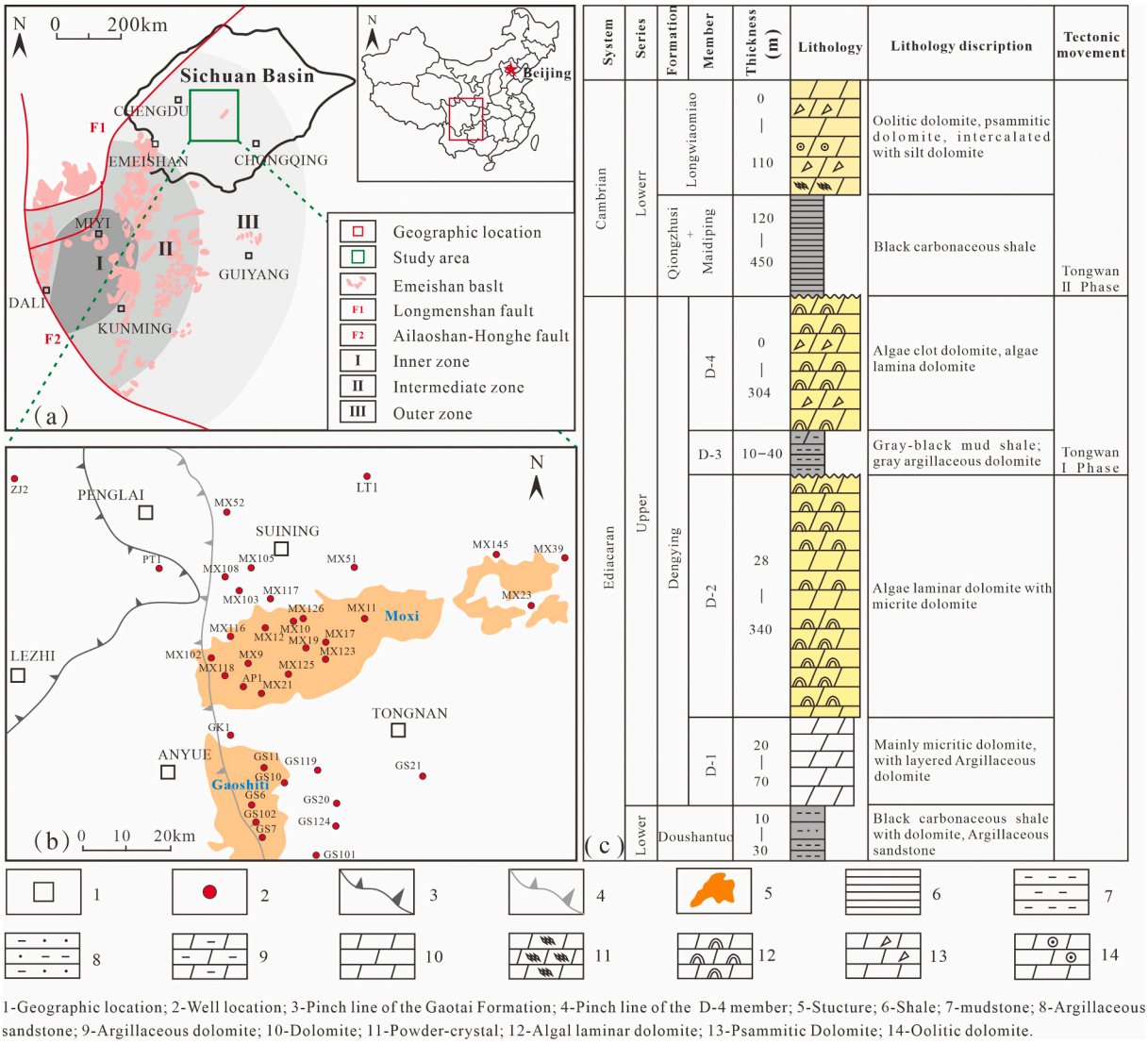

Fig. 1. Geological setting of the central Sichuan Basin. (a), (b) The location of the study area and the solid bitumen sampling wells (Modified based on He, 2016 and Lin et al., 2020); (c) The lithologic column in the central Sichuan Basin.

intergranular pores and dolomite intercrystalline pores (Zhou et al., 2015; Du et al., 2016; Hu et al., 2020; Tian et al., 2021). Studies have shown that large-scale paleo-oil reservoirs were developed in the DY and LWM formations in the central Sichuan Basin. Large amounts of pyrobitumen and natural gas are retained in the D-2 and D-4 members and the LWM Formation after crude oil cracking. (Zhu et al., 2015; Gao et al., 2017; Shi et al., 2017; Zhang, 2019).

The Emeishan Great Igneous Rock Province is located on the western edge of the Yangtze Craton. The Emeishan basalt is widely distributed in Yunnan, Guizhou, and Sichuan Provinces, with an exposed area of more than 50 × 10^4 km^2. The western region of the Emeishan basalts is bounded by the Ailaoshan-Honghe Fault, and the northwestern region by the Longmenshan Fault (He et al., 2003; He, 2016) (Fig. 1a). Studies have shown that the Emeishan basalt eruption began in the Late Permian and ended at 259.1 ± 0.5 Ma (lasting for 1 Ma) (Huang and Opdyke, 1998; Zhong et al., 2014). The activity of the Emeishan mantle plume was an extremely important thermal event in the Upper Yangtze area and led to a large area of hydrothermal activity on the southwestern edge of the Yangtze Plate, forming a large number of hydrothermal metal deposits (Boven et al., 2002; Zhang et al., 2013; Yuan et al., 2014). The axis of the Emeishan mantle plume is located in Miyi, Sichuan. Based on the different influences of the mantle plume on the strata, the Emeishan Great Igneous Rock Province can be divided into three zones from west to east: inner (deep denudation zone), intermediate (partial denudation zone), and outer (paleo-weathered crust) (He et al., 2003) (Fig. 1a). The study area is located in the outer zone. The mantle plume led to hydrothermal activity within the study area, leaving evidence of hydrothermal activity in the Permian, DY Formation, and other strata (Chen et al., 2012; Jiang et al., 2016a, 2016b; Feng et al., 2017; Jiang et al., 2018a, 2018b; Zhang, 2019).

3. Samples and methods

3.1. Rock thin sections preparation

Based on the core descriptions of 37 wells in the study area (Fig. 1a), more than 400 dolomite samples containing pyrobitumen in the D-2, D-4, and LWM reservoirs were selected. The rock samples were cut into smaller pieces with a cross-section of no more than 60 × 60 mm using a STX-1202A diamond wire cutting machine, and then cut into 20 × 20 mm pieces using a SYJ-200 cutting machine. The samples were subjected to coarse grinding using a UNIPOL-802 grinding and polishing machine, followed by fine grinding using alumina grit on a UNIPOL-802 grinding and polishing machine. Next, the samples were polished, using

1.0 and 0.3 um alumina suspensions, respectively, with a flannel polishing fabric. Subsequently, the samples were glued to glass slides using epoxy. After drying, the samples were ground to approximately 0.3 mm on a UNIPOL-1502 grinding and polishing machine, and the polishing process was repeated. Finally, the rock sections were prepared to investigate emplaced mineral characteristics, pyrobitumen optical textures, and the homogenization temperature of fluid inclusions. The preparation of rock thin sections follows the Chinese standard "Technical Specifications for Rock and Mineral Identification Part II: Sample Preparation of Rock Thin Sections" (DZ/T 0275.2-2015).

3.2. Pyrobitumen samples preparation

Based on the observation of a large number of rock thin sections, drilling cores containing the pyrobitumen with a single optical texture were selected for pyrobitumen preparation. The samples were collected near the location of the related thin sections to ensure that the optical texture of the obtained pyrobitumen was consistent with that of the thin section. To obtain pure solid bitumen samples, the solid bitumen-containing dolomite was broken into small pieces of 3–5 mm. Then, the solid bitumen particles (1–4 mm) were separated from the dolomite with wooden tweezers. A wooden tool was used to remove the dolomite, quartz, and other attached mineral fragments on the surface of the solid bitumen at 10× magnification under a microscope. The solid bitumen pieces were placed in a small beaker containing deionized water, and cleaned in 50 Hz ultrasonic waves for 1 h and dried in a drying oven at 80 °C for 5 h. Finally, an agate mortar was used to grind the solid bitumen pieces to 200 mesh for geochemical analysis.

3.3. Experimental method

3.3.1. Petrographic analysis

The pyrobitumen-enriched core samples and prepared thin sections were subjected to petrographic analysis. Macroscopic emplacement characteristics of hydrothermal minerals and pyrobitumen were observed from core samples. Microscopic emplacement characteristics of hydrothermal minerals and pyrobitumen and optical texture observation were conducted at the State Key Laboratory of Petroleum Resources and Prospecting at the China University of Petroleum (Beijing), using a Leica DM 4500P microscope equipped with a DFC 450C camera. The emplacement characteristics of hydrothermal minerals and pyrobitumen were observed in transmitted light. The optical structure of pyrobitumen was observed under reflected light.

3.3.2. Fluid inclusions

Fluid inclusion analysis was conducted at the Beijing Institute of Geology of Nuclear Industry, China. A LINKAM THMS600 heating-freezing stage was used to perform homogenization temperature analysis of the fluid inclusions. Temperature ranged from −195 to 600 °C, with a heating rate of 10 °C/min and cooling rate of 0.2 °C/min. Room temperature was set at 25 °C and the humidity at 50%. The fluid inclusion composition was analyzed by a Labram HR 800 research-grade micro-laser Raman spectrometer, and the laser was a Yag crystal frequency-doubled solid-state laser with a wavelength of 532 nm.

3.3.3. Organic element analysis

Organic elements in the solid bitumen (C, H, O, S, and N) were analyzed at the Shanxi Institute of Coal Chemistry, Chinese Academy of Sciences using an elemental analyzer (model Vario EL cube), with a room temperature of 26 °C and a humidity of 30% (following the Chinese standard GB/T19143-2017). The steps were as follows: In the CHNS mode of the elemental analyzer, 2–3 mg dried solid bitumen powder was burned in a pure oxygen atmosphere in a combustion tube. The produced gases were reduced to N_2, CO_2, H_2O, SO_2 and other gases, which were detected by the thermal conductivity detector in turn. Finally, the percentages of C, H, N, and S in the samples were calculated. In the O mode, the samples were put into a silver container and sent to a pyrolysis tube. The molecular bonds of oxides were broken under high temperature and oxygen-free conditions, and reacted with carbon powder to generate gases, such as CO, N_2, H_2, and CH_4. The CO was then adsorbed by the adsorption-desorption column and desorbed for detection after the impurity gases passed through the detector. Finally, the percentage of O in the sample was calculated.

3.3.4. Stable carbon isotope

Stable carbon isotope analysis was conducted at the Beijing Institute of Geology of Nuclear Industry, China, utilizing a Finnigan MAT 253 isotope mass spectrometer, and the analysis error was less than 0.1‰. The analysis results of stable carbon isotope were uniformly standardized using PDB (Peedee Belemnite) (‰).

3.3.5. Nuclear magnetic resonance (NMR)

The NMR analysis was conducted at the Shanxi Institute of Coal Chemistry, Chinese Academy of Sciences. NMR spectroscopy refers to the physical process of splitting the spin energy levels of atomic nuclei under an external magnetic field and resonantly absorbing a specific frequency of radiofrequency radiation. NMR is a powerful tool for identifying the structure and composition of compounds, which can quantify the types of carbon and hydrogen atoms in the bitumen molecules. The carbon NMR spectrum (^{13}C NMR) in this study was assessed by the 600 MHz superconducting solid-state NMR spectrometer, with an operating frequency of 151 MHz and a rotation speed of 10 k.

3.3.6. X-ray diffraction (XRD)

XRD was conducted at the Microstructure Laboratory for Energy Materials of China University of Petroleum (Beijing). XRD is one of the essential technical means for characterizing the microstructure of certain amorphous and crystalline materials and is widely used to analyze the crystal and molecular lamellar structures of carbonized and graphitized carbon materials. XRD analysis was performed using a Bruker D8 Focus X-ray diffractometer. The X-ray light source was a Cu target, ceramic light tube, with a power of 2.2 kV. A θ/2θ goniometer was applied, and a semiconductor array detector with 192 device channels was used. The scans ranged from 5° to 90°, and the scanning rate was 5°/min.

3.3.7. Thermogravimetry (TG)-mass spectrum

TG analysis provides information on the composition and thermal stability of solid compounds based on the relationship between sample weight and temperature under heating (Tao and Xu, 1987). In this study, it was used to assess the evolution of the internal structure of the pyrobitumen with different optical textures. The thermal stability of the pyrobitumen and the evolution of the gas generated from the system during heating were analyzed. The TG mass spectrum analysis was conducted at the Shanxi Institute of Coal Chemistry, Chinese Academy of Sciences. An Evolution 16/18 TG analyzer and OMNI star mass spectrometer were used for TG and gas composition analysis. TG analysis was performed in a nitrogen atmosphere (the N_2 flow rate was 100 mL/min), the heating rate was set to 10 °C/min, the final temperature was set to 1100 °C, and the TG resolution was 0.03 μg. The mass spectrometer was connected to the TG analyzer with a stainless steel capillary tube. A QMA 200 M analyzer and C-SEM Faraday detector were adopted, and the mass detection range was 1–300.

4. Results

4.1. Pyrobitumen characteristics

4.1.1. Emplacement characteristics

A large amount of pyrobitumen was developed in the DY reservoir, emplaced in the remaining algae framework pores, dissolved pores, and cracks (Fig. 2a-d). Observations of the pyrobitumen in the drilling cores

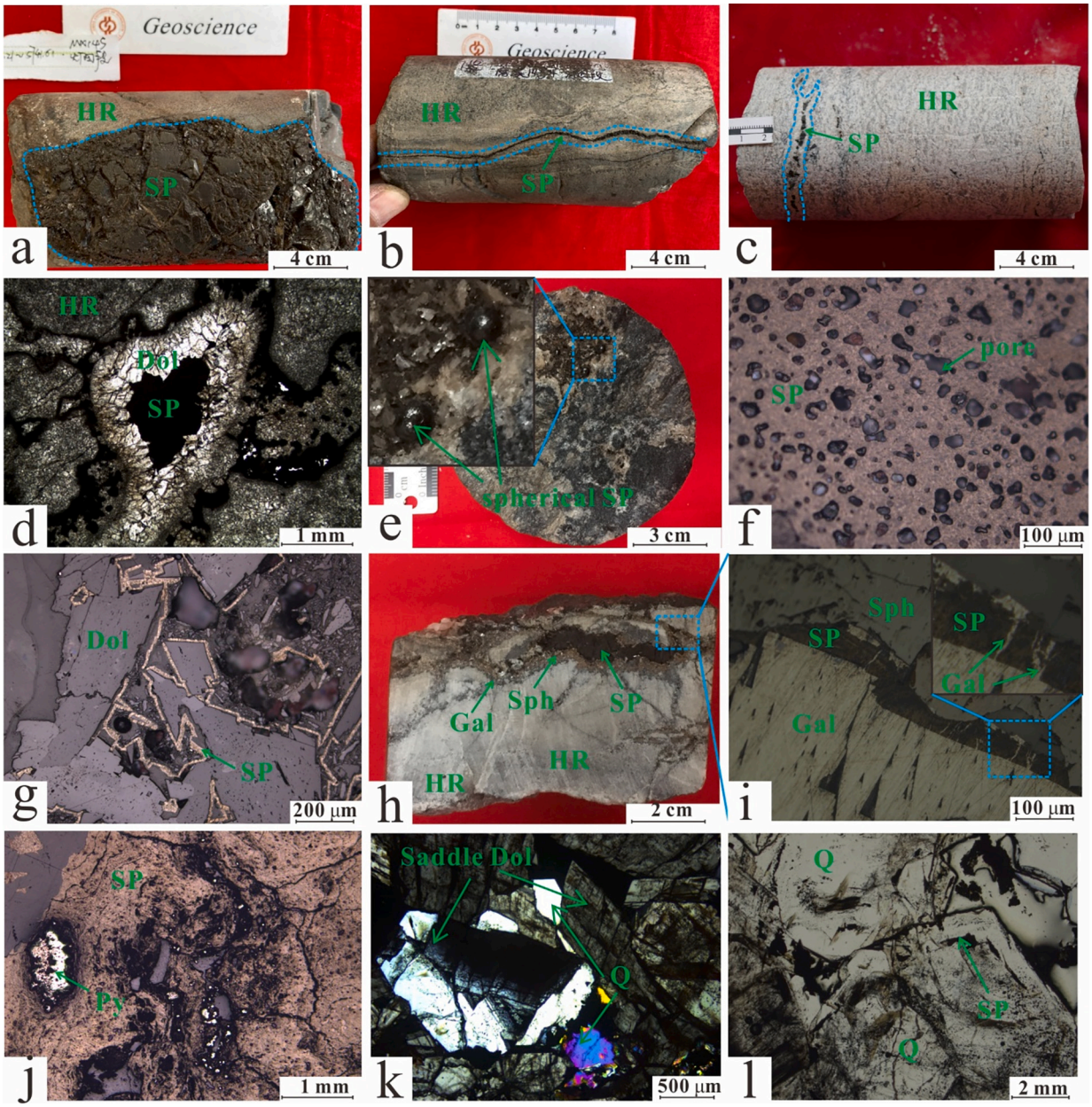

Fig. 2. Emplacement characteristics of pyrobitumen in the pore space of the DY and LWM reservoirs, the central Sichuan Basin.
HR = host rock; SP = solid pyrobitumen; Dol = dolomite; Sph = sphalerite; Gal = galena; Py = pyrite; Q = quartz. (a) MX145, 5741.21 m, D-4, the crack is emplaced with massive pyrobitumen. (b) MX145, 5741.21 m, D-4, with developed high-angle crack, and the crack is emplaced with pyrobitumen. (c) ZJ2, 6554.86 m, D-2, with developed algae framework pores (macro photo of algal framework pores in d), and the pore space is entirely emplaced with massive-structured pyrobitumen. (d) ZJ2, 6554.86 m, D-2, with developed algal framework pores, and the pore space is emplaced with fine-medium crystalline dolomite and pyrobitumen. (e) GS7, 5329.95 m, D-2, medium crystal dolomite and spherical-structured pyrobitumen are emplaced in the dissolved pores. (f) ZJ2, 6550.65 m, D-2, reflected and polarized light, pores are developed within pyrobitumen, and pore diameter < 50 μm. (g) PT1, 5748.28 m, D-2, reflected and polarized light, mesocrystalline dolomite is developed at the edge of the dissolved pore, and flaky-structured pyrobitumen is developed along the edge of the dolomites like a film. (h) GS7, 5293.44 m, D-4, a combination of sphalerite, galena, and solid bitumen is developed in the dissolved pores. (i) GS7, 5293.44 m, D-4, reflected and polarized light, a combination of sphalerite, galena and solid bitumen is developed in the dissolved pores. Galena is observed emplaced in the cracks of the pyrobitumen. (j) ZJ2, 6558.32 m, D-2, reflected and polarized light, massive pyrite is developed in the pyrobitumen. (k) PT1, 5789.72 m, D-2, transmitted and cross-polarized light, saddle-shaped dolomite and quartz are emplaced in the dissolved pores while pyrobitumen is emplaced in the intercrystalline pores. (l) PT1, 5727.67 m, D-2, transmitted and polarized light, massive quartz is emplaced in the pore space, and some pyrobitumen is trapped in the quartz.

and thin sections revealed that the pyrobitumen in the DY reservoir often exhibited massive (Fig. 2a-d), spherical (Fig. 2e) and thin lamellar structures (Fig. 2g). A small amount of massive-structured pyrobitumen had well-developed inner pores (diameter < 50 μm) (Fig. 2f). The massive-structured pyrobitumen was emplaced in the entire pore space (Fig. 2d), while the thin-skinned pyrobitumen developed along the pore edge in coating-form (Fig. 2g). These solid pyrobitumens often co-existed with hydrothermal minerals, such as pyrite, sphalerite, galena, saddle dolomite, and quartz (Fig. 2h-l). The emplaced mineral sequence showed that the pyrobitumen was located in the intercrystalline pores of saddle dolomite (Fig. 2k) and within the galena and quartz (Fig. 2i, l), indicating that the pyrobitumen formed later than the saddle dolomite but earlier than the galena and quartz.

4.1.2. Optical texture

In this study, based on the optical texture under the reflected-light

microscope, the pyrobitumen of the DY-Lower Cambrian reservoirs was categorized into three categories: isotropic, mosaic and fibrous (Patrick et al., 1973; Sanada, 1978; Grint et al., 1979; White and Price, 1974) (Fig. 3). Isotropic pyrobitumen contains no particles (Fig. 3a–c). Anisotropic particles were found in mosaic pyrobitumen (Fig. 3d–i), while fibrous bitumen exhibited alternating dark and bright bands (Fig. 3j–l), which may result from the collapse of bubbles formed from volatile components (White, 1976; Stasiuk, 1997; Rimmer et al., 2015). Because, in highly-mature stage, the volatile component would form bubbles in the pyrobitumen (White, 1976). The nucleation, growth, and percolation of bubbles would produce the plastic deformation of the soft pyrobitumen (White, 1976; Stasiuk, 1997). After the bubbles collapsed, the layered bubble walls would display a fibrous optical texture (White, 1976; Stasiuk, 1997; Yang et al., 2018). According to the size of the anisotropic particles, mosaic pyrobitumen can be further divided into FM, MM and CM. The anisotropic particles in the FM pyrobitumen are

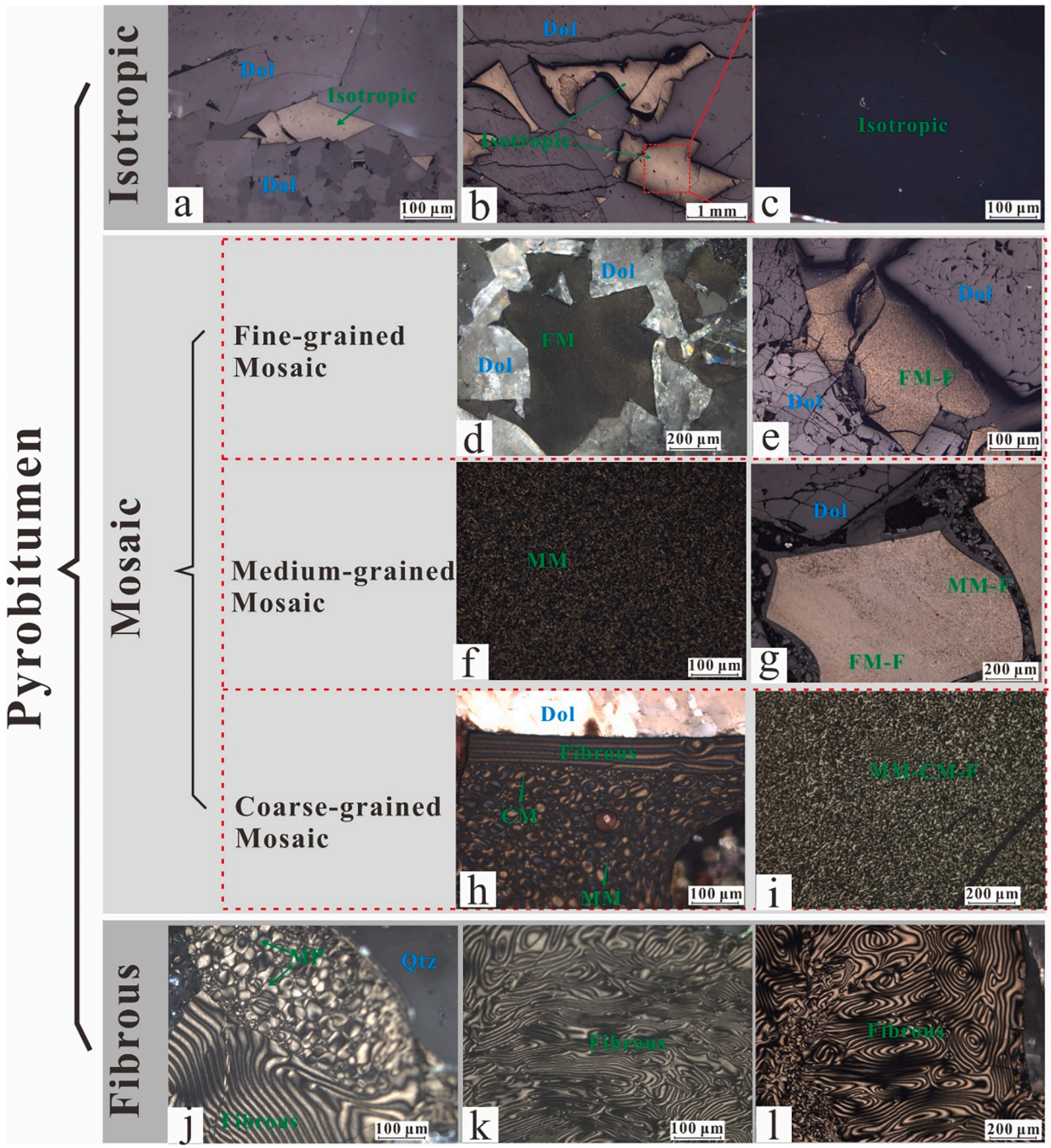

Fig. 3. Optical textures of the pyrobitumen in the DY and LWM reservoirs.
Photos were taken under reflected light. (a) MX13, 4581.3 m, LWM, polarized light, isotropic pyrobitumen; (b) MX11, 4877.4 m, LWM, polarized light, isotropic pyrobitumen; (c) MX11, 4877.4 m, LWM, cross-polarized light, isotropic pyrobitumen; (d) MX145, 5822.15 m, D-4, cross-polarized light, fine-grained mosaic (FM) pyrobitumen; (e) PT1, 5729.44 m, D-2, polarized light, fine-grained pyrobitumen near the fibrous pyrobitumen (FM-F) in h; (f) MX23, 5210.72 m, D-4, cross-polarized light, medium-grained mosaic (MM) pyrobitumen; (g) PT1, 5733.89 m, D-2, polarized light, fine-grained and medium-grained mosaic pyrobitumen near the fibrous pyrobitumen (FM-MM-F) in h; (h) GS20, 5183.47 m, D-4, cross-polarized light, coarse-grained mosaic (CM) pyrobitumen with some fibrous pyrobitumen; (i) GS124, 5547.57 m, D-4, cross-polarized light, medium-coarse-grained mosaic pyrobitumen near the fibrous pyrobitumen (MM-CM-F) in l; (j) MX145, 5575.00 m, D-4, cross-polarized light, fibrous pyrobitumen and unfused mesophase spheres (MP); (k) PT1, 5745.89 m, D-2, cross-polarized light, fibrous pyrobitumen; (l) GS7, 5274.11 m, D-4, cross-polarized light, fibrous pyrobitumen.

smaller than 1 μm, exhibiting slightly anisotropic texture under the microscope (Fig. 2d). The MM pyrobitumen contains anisotropic particles with diameters ranging from 1 to 5 μm (Fig. 2f), while the CM pyrobitumen has anisotropic particles larger than 5 μm (Fig. 2h). In exploration wells where fibrous pyrobitumen is developed, such as PT1 and GS124, FM, MM, and CM pyrobitumen are alternately developed with fibrous pyrobitumen. These mosaic pyrobitumens alternately developed with fibrous pyrobitumen were denoted as FM-F, MM-F, and CM-F, respectively (Fig. 3e, g, i; Fig. 12).

4.2. Fluid inclusions

Many aqueous and hydrocarbon inclusions were found in the saddle dolomite and quartz (Fig. 4). The hydrocarbon inclusions consists of dark grey natural gas inclusions, distributed in a belt-like shape with the symbiotic aqueous inclusions along the mineral growth direction (Fig. 4c, f). Raman analysis shows that the main component of the natural gas inclusions is CH_4 (Fig. 5). The gas-liquid ratio of the aqueous inclusions in the saddle dolomite is approximately 10%; the salinity exceeds 16 wt% NaCl eqv (Fig. 6). The aqueous inclusions captured in the quartz have a gas-liquid ratio of 10% and a salinity of 18–20 wt% NaCl eqv (Fig. 6). The aqueous inclusions captured in the barite had a gas-liquid ratio of 10% and a salinity of 18–20 wt% NaCl eqv (Zhang, 2019). The gas-liquid ratios and salinities of the aqueous inclusions captured in the three hydrothermal minerals were similar, with a homogenization temperature ranging from 220 to 340 °C (Fig. 6). The fluid inclusions captured by the three hydrothermal minerals displayed high temperature and salinity characteristics.

4.3. Organic elements

The organic elements in the pyrobitumen are primarily C, H, O, N, and S. The C concentration in all pyrobitumen samples exceeds 80%, with a mean value of 83.14% (ranging from 80.69% to 85.64%). The O concentration varies from 3.11% to 5.21%, with a mean value of 4.22%. The H concentration ranges from 2.22% to 2.85%, with a mean value of 2.45%. The N concentration is approximately 0.65% (ranging from 0.54% to 0.78%), while the S concentration is approximately 7.88% (ranging from 6.64% to 8.95%) (Table 1). The H/C ratio ranges from 0.31 to 0.41, and the O/C ratio varies from 0.03 to 0.05 (mean value: 0.04). This demonstrates that the pyrobitumens have undergone high degree of dehydration and thermal stress and are in the overmature stage.

There are specific differences in the H/C ratios of the pyrobitumens with different optical textures. Isotropic pyrobitumen has the highest H/C ratio (approximately 0.41). As the optical texture of pyrobitumen changes from: isotropic → FM → MM → CM → fibrous, the H/C ratio gradually decreases to 0.34. In addition, the mosaic pyrobitumen alternating with the fibrous bitumen has the lowest H/C ratio (approximately 0.32).

4.4. Stable carbon isotopes

There are three types of pyrobitumen (FM, FM-MM and fibrous pyrobitumens) developed in the D-2 member of the well PT1. The FM and FM-MM pyrobitumens are alternately developed with the fibrous pyrobitumen (indicated as FM-F and FM-MM-F, respectively).

The carbon isotope value of the fibrous pyrobitumen ranges from −36.5‰ to −38.3‰, with a mean value of −37.4‰, that of the FM-MM-F pyrobitumen has a mean value of −36.9‰ (ranging from −36.7‰ to -37.1‰), and that of the FM-F pyrobitumen has a mean value of −34.7‰ (ranging from −33.7‰ to −35.4‰) (Table 2). The carbon isotopes of the FM-MM pyrobitumen are lighter than those of the FM-F pyrobitumen (0.5‰ lighter), while the carbon isotopes of the fibrous pyrobitumen are lighter than those of the FM-F and FM-MM-F pyrobitumens (2.7‰ and 2.2‰ lighter, respectively).

4.5. Carbon NMR

Carbon NMR spectroscopy (^{13}C NMR) was used to study the carbon skeleton structure of pyrobitumen. The different chemical shift intervals in the map can be attributed to six different structural, functional groups: non-polar aliphatic carbon (62–0 ppm), oxygen-attached fatty carbon (92–62 ppm), aromatic carbon (150–92 ppm), oxygen-attached

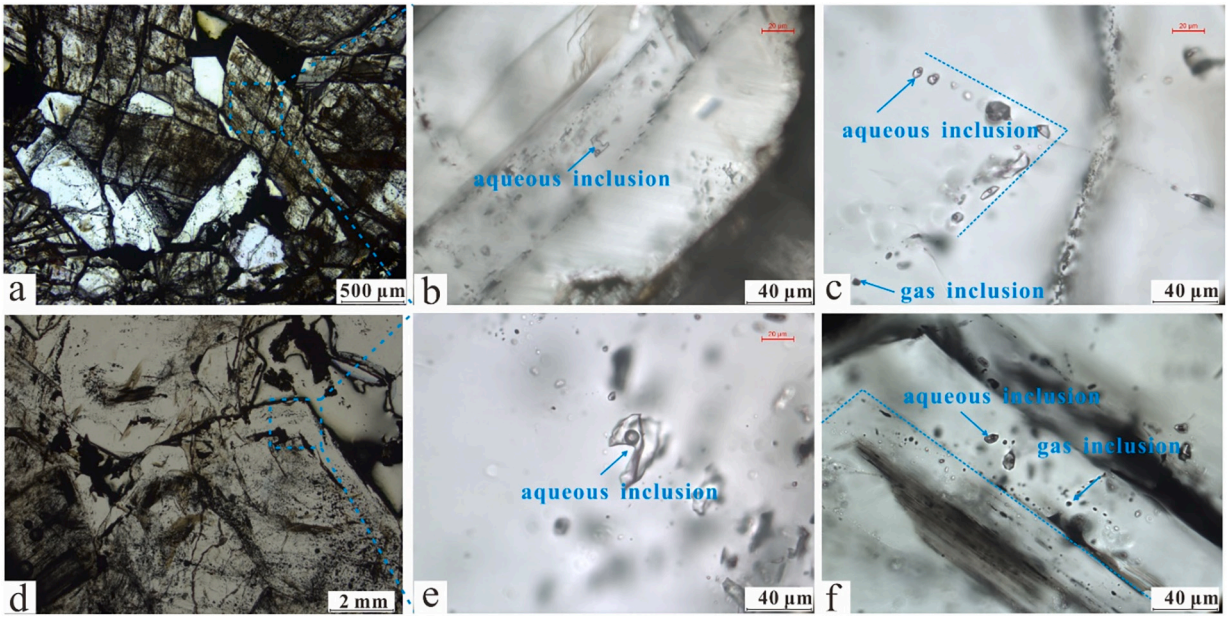

Fig. 4. Fluid inclusions captured by the hydrothermal minerals in the DY and LWM Formation reservoirs.
Photos were taken in transmitted light. (a–c) PT1, 5789.72 m, D-2, a was from cross-polarized light, b and c were from polarized light, dark grey gaseous hydrocarbon-inclusions and aqueous inclusions are captured in the saddle dolomite, and fluid inclusions are distributed along the mineral growth direction in a belt-shape; (d–f) PT1, 5727.67 m, D-2, polarized light, dark grey gaseous hydrocarbon-inclusions and aqueous inclusions are captured in the large blocks of quartz, and the fluid inclusions are distributed along the mineral growth direction.

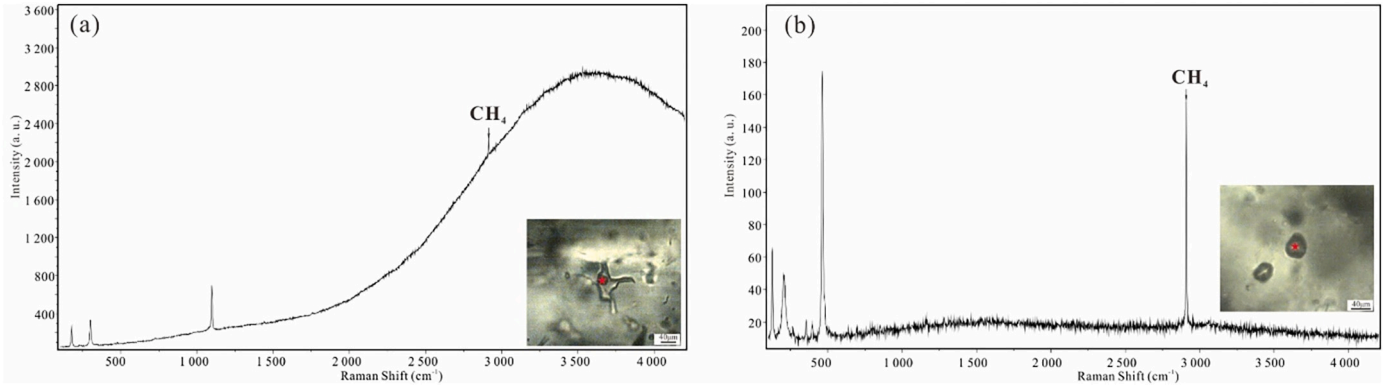

Fig. 5. Raman spectra of the fluid inclusions captured by hydrothermal minerals.
(a) Two-phase aqueous inclusion captured by saddle dolomite; the gas phase is primarily composed of CH_4; (b) Natural gas inclusion that is captured by quartz; the natural gas is primarily CH_4.

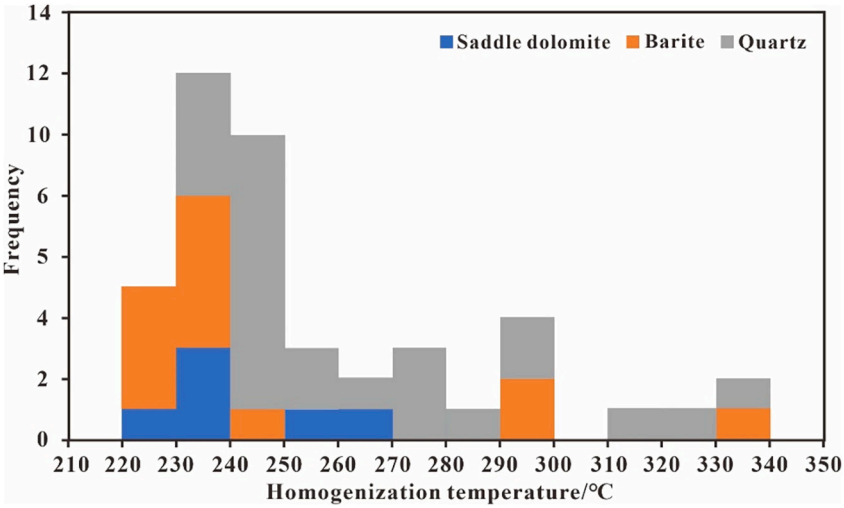

Fig. 6. Homogenization temperature of the aqueous inclusions captured in the hydrothermal minerals in the DY and LWM formations (data of fluid inclusions in barite and a portion of those in quartz were quoted from Zhang, 2019).
The homogenization temperatures of the aqueous inclusions in the saddle dolomite range from 220 to 280 °C, those in the quartz range from 230 to 340 °C, and those in the barite range from 220 to 340 °C.

Table 1
Elemental analysis of pyrobitumen in the DY and LWM reservoirs (dry basis, H/C, S/C, and O/C refer to the atomic ratios).

Samples	Depth/m	Optical texture	N	C	H	S	O	H/C	S/C	O/C
			%							
MX13–1	4581.30	Isotropic	0.70	82.81	2.85	8.13	\	0.41	0.04	\
MX13–2	4581.40		0.67	82.88	2.77	8.66	\	0.40	0.04	\
MX108–1	5330.30	FM	0.68	80.72	2.60	8.95	5.21	0.39	0.04	0.05
MX108–2	5330.50		0.71	80.69	2.56	8.76	5.06	0.38	0.04	0.05
PT1–8	5733.89	FM-MM-F	0.64	84.32	2.24	8.43	3.21	0.32	0.04	0.03
PT1–8-2	5734.10		0.62	84.37	2.25	8.55	3.11	0.32	0.04	0.03
LT1–1	5471.80	MM	0.78	82.83	2.54	7.78	4.05	0.37	0.04	0.04
LT1–2	5471.90		0.76	82.80	2.54	7.96	4.05	0.37	0.04	0.04
MX125–1	5334.70	MM-CM	0.61	83.56	2.47	8.14	\	0.36	0.04	\
MX125–2	5334.80		0.60	83.51	2.49	7.91	\	0.36	0.04	\
GS124–1	5547.60	MM-CM-F	0.67	85.64	2.25	7.02	\	0.32	0.03	\
GS124–2	5547.70		0.65	85.15	2.22	7.10	\	0.31	0.03	\
GS6–1	5367.20	Fibrous	0.62	84.33	2.44	6.75	4.73	0.35	0.03	0.04
GS6–2	5367.30		0.62	84.58	2.42	6.64	4.64	0.34	0.03	0.04
GS20–1	5195.20		0.58	83.26	2.46	7.29	4.88	0.36	0.03	0.04
GS20–2	5195.30		0.54	83.31	2.42	7.40	4.83	0.35	0.03	0.04
PT1–12	5727.67		0.64	80.89	2.27	8.17	3.38	0.34	0.04	0.03
PT1-12-2	5727.80		0.64	80.88	2.25	8.17	3.44	0.33	0.04	0.03

aromatic carbon (165–150 ppm), hydroxyl carbon (190–165 ppm) and carboxyl carbon (220–165 ppm) (Wang et al., 1995; Werner-Zwanziger et al., 2005; Mao et al., 2010).

Carbon NMR analysis of pyrobitumens with different optical textures show that the absorption peak in the ^{13}C NMR spectrum of the pyrobitumen concentrates in the aromatic carbon region (fa, 92–150 ppm) (Fig. 7), indicating that the carbon skeleton of the pyrobitumen primarily has aromatic carbon structure. The anisotropy of the aromatic

Table 2
$\delta^{13}C$ (stable carbon isotope) of the pyrobitumen in the D-2 member from well PT1.

Samples	Depth/m	Optical texture	^{13}C/PDB/‰
PT1–12	−5727.67	Fibrous	−37.7
PT1–11	−5729.44	FM	−33.7
PT1–10	−5730.03	FM	−35.4
PT1–9	−5733.28	FM-MM	−35.0
PT1–8	−5733.89	FM-MM	−36.9
PT1–7	−5741.06	FM-MM	−37.1
PT1–6	−5744.95	FM-MM	−36.7
PT1–5	−5746.51	Fibrous	−36.7
PT1–4	−5778.20	Fibrous	−37.7
PT1–3	−5779.53	Fibrous	−36.5
PT1–2	−5780.74	Fibrous	−37.3
PT1–1	−5790.26	Fibrous	−38.3

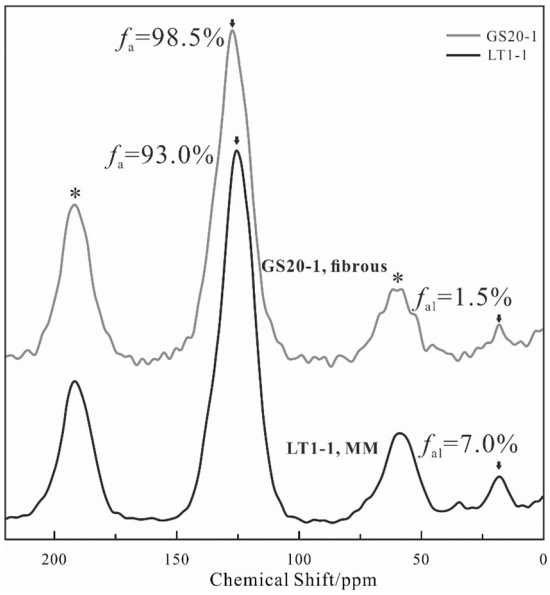

Fig. 7. ^{13}C NMR spectrogram of the pyrobitumen in the DY Formation.
The aromatic carbon concentration (fa) of the MM pyrobitumen is about 93%, while the saturated carbon concentration (fal) is about 7.0%. The aromatic carbon concentration (fa) of the fibrous pyrobitumen is about 98.5%, while the saturated carbon concentration (fal) is about 1.5%.

carbon chemical shift results in obvious rotating sidebands near 60 and 200 ppm (Yang, 2011). The concentrations of aromatic carbon in the two tested pyrobitumen samples were very high (Fig. 7). The pyrobitumen was formed by aromatic compounds with aromatic carbon as the skeleton, and there are only limited alkyl substituents in the pyrobitumen, which is consistent with the low H/C ratio. In addition, there were specific differences in the skeleton structures of pyrobitumens with different optical textures. NMR analysis reveals that fibrous pyrobitumen has a higher aromatic carbon concentration than the MM pyrobitumen (Fig. 7), showing a higher degree of condensation polymerization, which is consistent with its lower H/C ratio (Table 1).

4.6. X-ray diffraction (XRD)

According to the diffraction angle at C (002), the crystal interlayer spacing d_{002} is calculated as follows (Bouhadda et al., 2007):

$$d_{002} = \lambda / 2sin\theta \quad (1)$$

where θ is the diffraction angle (Bragg angle $2\theta \approx 42.48°$), and λ is the X-ray light wavelength ($\lambda = 1.5406$);

The graphitization degree was calculated according to the empirical formula (Li et al., 2005):

$$G = (0.3440 - d_{002})/(0.3440–0.3354) \quad (2)$$

where d_{002} is the interlayer spacing at C (002); the interlayer spacing at C (002) of the fully ungraphitized carbon crystal is 0.3440 nm; the interlayer spacing at C (002) of the natural graphite is 0.3354 nm.

The molecular distribution in the mesophase can affect the orientation and arrangement of the aromatic layer in the mesophase. The peak positions and morphologies for pyrobitumens with different optical textures were very similar, showing characteristic peaks of 002 and 100 crystal planes in the graphite near 2θ values of 26° and 43°. This indicates that all pyrobitumen samples contained microcrystals with similar graphite structures (Fig. 8). The peaks of the 002 crystal planes in each reservoir were relatively sharp, indicating that the lattice arrangement of the pyrobitumen was regular and orderly, the parallel arrangement of the aromatic layers was highly ordered, and the crystallinity was good.

The microcrystalline parameters of pyrobitumen exhibited certain differences with different optical textures. The fibrous pyrobitumen had the smallest carbon interlayer spacing (d_{002}) (mean value: 0.3398 nm, ranging from 0.3397 to 0.3400 nm) and the highest degree of graphitization (mean value: 48%, ranging from 47% to 50%). In contrast, the isotropic pyrobitumen had the largest spacing (approximately 0.3415 nm), and its degree of graphitization was the lowest (approximately 29%) (Table 3). The carbon interlayer spacing of mosaic pyrobitumen was intermediate to the former two. For the mosaic pyrobitumen, the carbon interlayer spacing of the MM-CM pyrobitumen was the smallest (approximately 0.3404 nm), and their degree of graphitization was approximately 42%. The carbon interlayer spacings of the MM and FM pyrobitumens were similar (approximately 0.3407 nm), larger than that of the MM-CM pyrobitumen, and their degree of graphitization was 39%. The carbon interlayer spacing of mosaic pyrobitumen alternately developed with the fibrous pyrobitumen was the largest (approximately 0.3410 nm), and its graphitization degree was 36%. Overall, the pyrobitumens with various optical textures have a high degree of order in the aromatic layer and regular crystal lattice arrangement, preferred orientation, and high crystallinity. They have evolved into semi-graphitized pyrobitumen.

4.7. Thermogravimetric (TG)-mass spectrum

In heating to 1100 °C, the TG curve of all pyrobitumen samples were similar. As the temperature increased, the weight of the pyrobitumen samples gradually decreased, and the final carbon residue rate of all samples was above 89% (Fig. 9a).

Studies have shown that the thermal weight loss process of solid bitumen can be summarized by three stages of heating (Song, 1996; Alvaraz et al., 2008; Fanjul et al., 2003): (1) The volatilization process of small molecular components (such as CH_4, H_2O) from the solid bitumen in the system with the continuous increase of temperature; (2) the liquid-phase carbonization of solid bitumen. In this process, the side chain of the alkyl group in the pitch will be broken, decomposed, and reacted with free radicals and thermal polycondensation. As a result, by-products with minor molecules (such as CH_4 and C_2H_6) are generated, and they escape, which is the main factor of weight loss; and (3) the solid-phase carbonization stage. Severe weight loss no longer occurs at this stage, only part of the alkyl side chain will be broken, and little gas is generated. Our weight loss results are consistent with those of previous studies (Fanjul et al., 2003; Alvaraz et al., 2008; Tian et al., 2013). In the pyrobitumen samples in this study, weight loss primarily occurred in two intervals of temperature: 0–300 °C and 600–900 °C. After exceeding 900 °C, the severe weight loss ended (Fig. 9).

To clarify whether the reasons for weight loss in the natural pyrobitumen samples in the studied reservoir are consistent with those reported in previous studies, mass spectrometric analysis of the gas produced by the pyrobitumen during the heating process was also

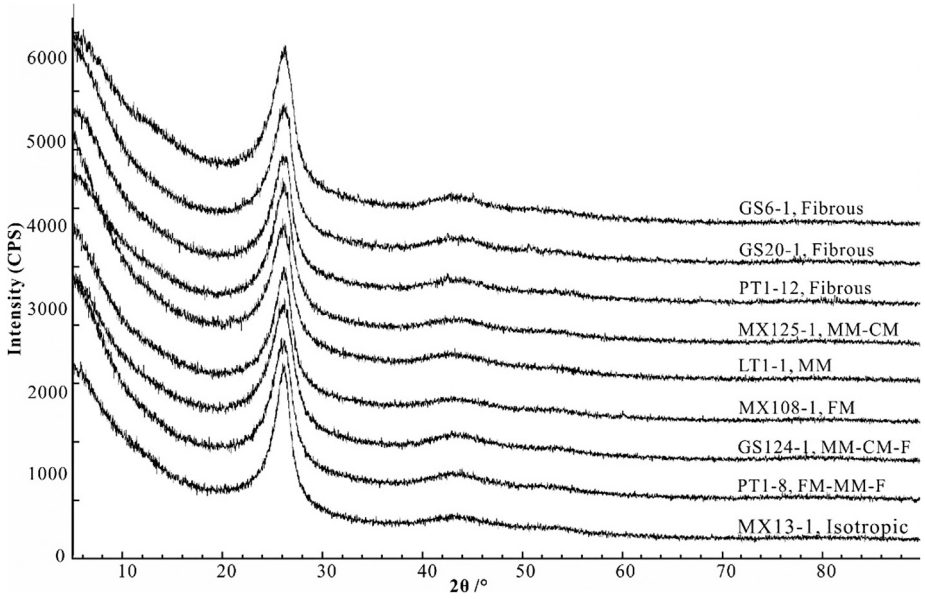

Fig. 8. XRD pattern of the pyrobitumens in the DY and LWM Formation.

Table 3
XRD parameters of the pyrobitumens in the DY and LWM Formations.

Samples	Depth/ m	Optical texture	2θ/°	d_{002}/ nm	Graphitization/ %
MX13–1	4581.30	Isotropic	26.06	0.3415	29
MX108–1	5330.34	FM	26.13	0.3407	39
PT1–8	5733.89	FM-MM-F	26.09	0.3412	33
LT1–1	5471.82	MM	26.13	0.3407	39
MX125–1	5334.70	MM-CM	26.15	0.3404	42
GS124–1	5547.60	MM-CM-F	26.13	0.3407	39
GS6–1	5367.16		26.19	0.3398	48
GS20–1	5195.15	Fibrous	26.18	0.3400	47
PT1-12	5727.67		26.2	0.3397	50

conducted. The results showed that the weight loss of pyrobitumen during heating was caused by the loss of light components such as CH_4, H_2, and H_2O. Fig. 10 shows that for the temperatures less than 300 °C, the gases that escaped from the pyrobitumen were primarily CH_4, H_2, and H_2O (Fig. 10). When the system temperature reached 100 °C, gases such as CH_4 and H_2 were expelled (Fig. 10). The pyrobitumen samples have experienced high temperatures exceeding 200 °C throughout their geological history (Xu, 2017; Su et al., 2020); therefore, H_2O, CH_4, and H_2 were not produced during cracking but released from the adsorbed water and gas.

After the heating temperature exceeded 600 °C, minor molecular gases such as CH_4 and H_2 appeared in the system, which was an important cause of weight loss in the pyrobitumen at this stage (Fig. 10). The H_2 and CH_4 escaping at this temperature (>600 °C) is considered to be generated from pyrolysis and polycondensation of solid bitumen (Lewis, 1987; Song, 1996; Fanjul et al., 2003; Wu, 2006; Alvaraz et al., 2008). In the range of 300–600 °C, the weight loss rate of pyrobitumen was low, and there were no cracking products, like CH_4, H_2 and other small molecules, indicating that the internal structure was relatively stable (Fig. 10).

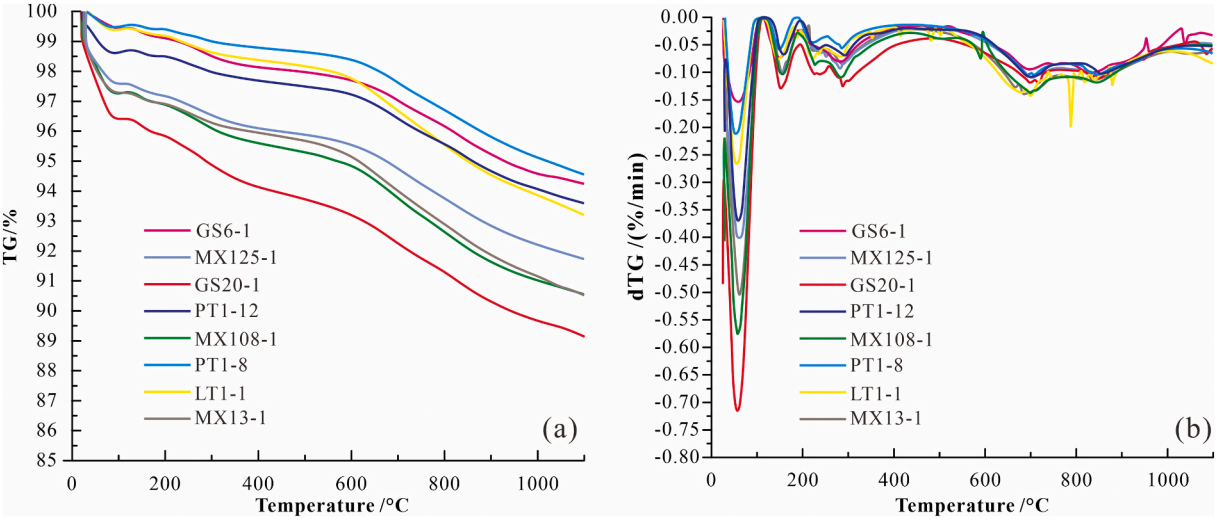

Fig. 9. TG and DTG curves of the reservoir pyrobitumen samples.

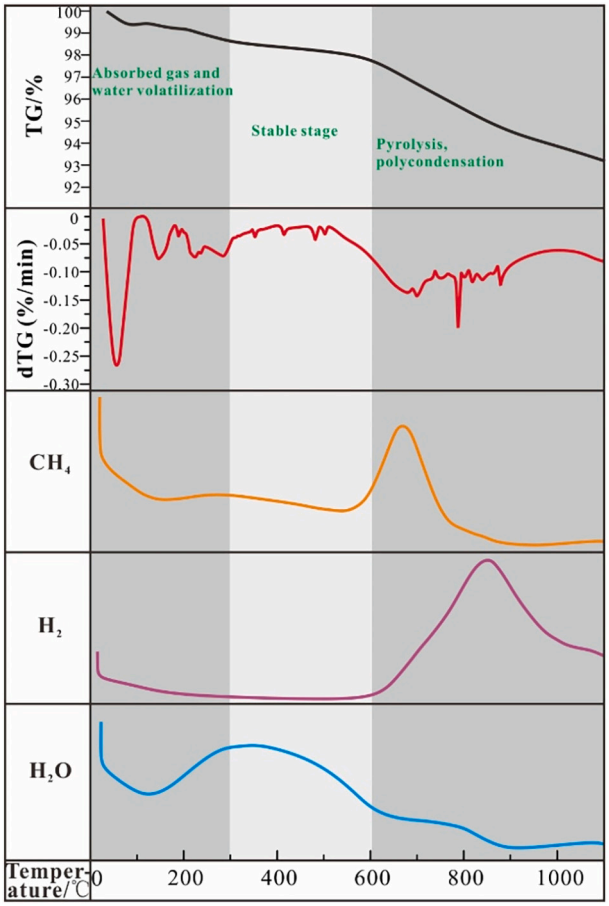

Fig. 10. Composition of the gases released from the pyrobitumen at different temperatures.
From 0 to 300 °C, the escaped gas was mainly CH4, H2, and H2O; 300–600 °C, the pyrobitumen was relatively stable, and almost no gas escaped; 600–900 °C, the escaped gas was primarily CH4 and H2; exceeding 900 °C, only a small amount of H2 escaped.

5. Discussion

5.1. Evidence of hydrothermal activity

5.1.1. Evidence from the fluid inclusions

Hydrothermal activities result in the generation of hydrothermal minerals such as sphalerite, galena, pyrite, and barite, which usually appear together (Inoue, 1995; Jiang et al., 2019). In the DY reservoir, large amounts of sphalerite, galena, pyrite, barite, and other hydrothermal minerals are *emplaced* in the pore space (Fig. 2), co-existing with pyrobitumen, suggesting that the DY reservoir may have experienced hydrothermal activity. Burial history shows that DY Formation did not experience a maximum paleotemperature over 220 °C (Gao et al., 2018; Xu, 2017; Su et al., 2020). However, the homogenization temperature of the fluid inclusions shows that when saddle dolomite, quartz, barite and other minerals crystallized, the strata temperature of the DY Formation exceeded 220 °C, and even reached 340 °C (Fig. 6). This is the strongest evidence indicating that the DY Formation was affected by hydrothermal activity whose temperature was not lower than 340 °C. Saddle dolomite and quartz were formed at different stages of the hydrothermal activity, while the formation of pyrobitumen occurred between the two (Fig. 2i, k, l); thus, the pyrobitumen was formed during hydrothermal activity.

5.1.2. Evidence from the optical textures of pyrobitumen

Temperature and pressure are the most important parameters affecting the formation of mesophase pitch (Goodarzi, 1985; Yokono et al., 1986; Fathollahi et al., 2005; Eksilioglu et al., 2006; Sun et al., 2020). In this study, numerous optically anisotropic pyrobitumens with mosaic and fibrous structures co-existed with isotropic pyrobitumen. The anisotropic pyrobitumen has experienced the highest paleo-temperature, over 300 °C. This is also strong evidence that the DY Formation reservoir has experienced hydrothermal activity, which is consistent with the temperature analysis of the fluid inclusions.

5.2. Controlling factors of the optical texture of pyrobitumen

Research on petroleum coke indicates that the optical anisotropy or textures of the pyrobitumen depend on the properties of the precursor and the physical conditions of coking. In the process of "coking" under natural conditions, the development of the optical texture is controlled by the properties of the precursor and the system temperature and pressure (Marsh and Cornford, 1976; White, 1976; Goodarzi, 1985; Stasiuk, 1997; Rimmer et al., 2015). Based on the analysis of previous study results about burial depth and formation pressure of the DY Formation, it is found that the formation pressure of the DY Formation in the study area during the oil cracking period was similar across the area (Wei et al., 2015b; Liu, 2018). Therefore, pressure was not the main factor controlling the optical structure of the pyrobitumen, and the properties of the precursor and the system temperature were the focus of this study.

5.2.1. Heteroatoms and optical texture of pyrobitumen

Heteroatoms (O, S, N, etc.), with the exception of C and H in the precursor, will affect the formation and development of mesophase pyrobitumen. When the oxygen concentration exceeds 7%, mesophase spheres cannot be formed (Mochida et al., 1980; Liu et al., 2003a, 2003b). Excessive S concentration is also not conducive to the fusion of mesophase spheres. Mochida et al. (1980) carbonized two types of raw materials containing a small number of S compounds (thioxanthene and thianthene) and found that only mosaic pyrobitumen could be formed. The effect of the N-containing compounds on mesophase generation during carbonization is similar to that of S.

The O concentration of all pyrobitumens in the study area was less than 7%, which meets the conditions required for mesophase generation. The concentrations of S, O, N, and other elements in the fibrous pyrobitumen are not significantly different from those in the FM and MM pyrobitumen (Fig. 11), demonstrating that the heteroatom concentrations in central Sichuan did not affect the optical texture.

5.2.2. The components and optical texture of pyrobitumen

Observation of the drilling core of well PT1 in the DY Formation shows that the pyrobitumen is primarily fibrous. However, FM-F and FM-MM-F pyrobitumens also developed in some sections, alternating with fibrous pyrobitumen (Fig. 12). The emplaced locations of these three pyrobitumens are similar (Fig. 12), and their geological temperatures were similar, indicating that the difference in optical texture was not caused by temperature. FM-F and FM-MM-F pyrobitumens developed at the bottom of the high-porosity section of the D-2 reservoir, with heavier carbon isotopes than those in the fibrous pyrobitumen (Fig. 12). Similarly, Stasiuk (1997) found this phenomenon in the Devonian Leduc Formation reservoir in central Alberta. He explained that it was due to the tar mat developed in the reservoir. Asphaltenes and other high molecular weight hydrocarbons can concentrate in the high-porosity sections of reservoirs as tar mats due to processes related to oil mixing (multiple charging) and gravity segregation during filling of reservoirs or from oil deasphalting promoted by a reduction in asphaltene solubility from gas charging (Wilhelms and Larter, 1995; Rimmer et al., 2015). There were specific differences in the isotopes of saturated hydrocarbons, aromatic hydrocarbons, and asphaltene in crude oil: $^{13}C_{Asphaltene} > {}^{13}C_{Aromatic} > {}^{13}C_{Saturated}$. The enrichment of asphaltenes in the tar mat led to heavier carbon isotopes. The mosaic pyrobitumens,

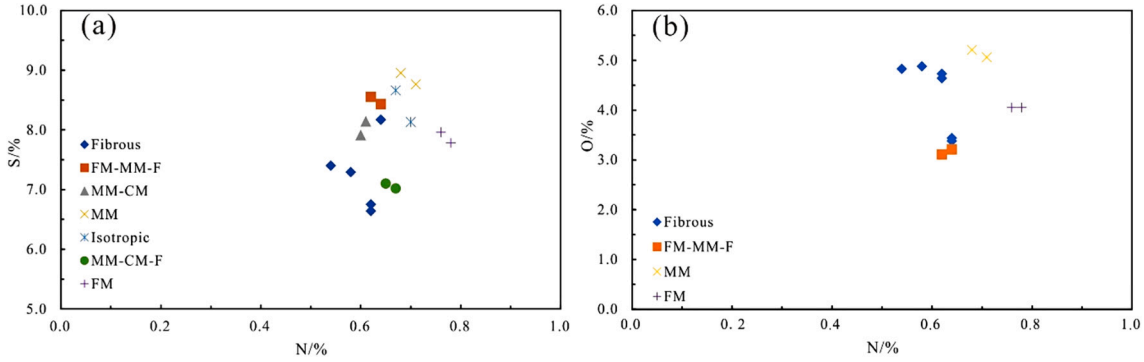

Fig. 11. The concentration characteristics of S, N and O of the pyrobitumen in the DY and LWM formations.
The concentrations of S, N, and O in the pyrobitumen with various optical textures are equivalent, with similar distribution zones.

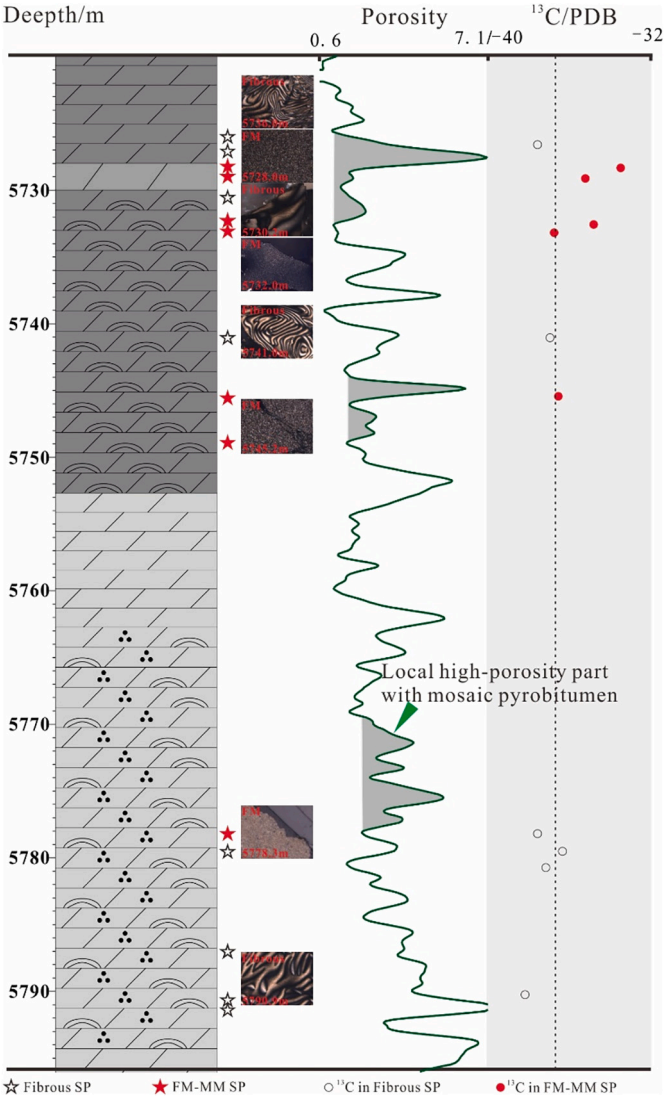

Fig. 12. Optical texture and ^{13}C distribution map of the pyrobitumen in the D-2 Member of well PT1.
The reservoir was primarily emplaced with fibrous pyrobitumen, and FM-MM pyrobitumen was observed at the bottom of the high porosity section. The ^{13}C value of the fibrous pyrobitumen is relatively lower than that of the FM-MM pyrobitumen.

alternately developed with fibrous pyrobitumens, had heavier carbon isotopes and developed in the high-porosity section of the reservoir, which is similar to the tar pad characteristics reported by Stasiuk (1997) (Fig. 12). The precursors of the mosaic pyrobitumen alternately developed with fibrous pyrobitumen were the tar mats formed by the enrichment of asphaltenes and other hydrocarbons with high molecular weight.

Based on the analysis of the elemental composition and XRD results of the mosaic pyrobitumens, the mosaic structure is thought to be caused by the enrichment of primary QI. The primary QI in the solid bitumen is a polymer particle composed of a fused-ring polymer compound with considerable molecular weight and a small amount of ash, with high carbon and low hydrogen characteristics (Sun et al., 2020). QI has a high molecular weight and is easily to concentrate with asphaltenes in high-porosity section of the reservoirs as tar mats. The QI can reduce the pre-exponential factor and transformation activation energy of the mesophase, which is conducive to its nucleation. However, as the number of small mesophase spheres increases, they will gather on the surface of the spheres, preventing them from approaching and fusing, finally resulting in the formation of only mosaic pyrobitumen (Qian et al., 1984; Li and Li, 1996; Zhang, 2007). The enrichment of QI reduces the H/C ratio of the pyrobitumen and inhibits the fusion of mesophase spheres. As a result, the QI enriched pyrobitumen with a tar mat precursor, which is emplaced in the high-porosity section, exhibits a mosaic structure with a low H/C ratio. In addition, the carbon interlayer spacings of the FM-F and FM-MM-F pyrobitumens are significantly larger than that of the adjacent fibrous pyrobitumen, while their degrees of graphitization is lower. It demonstrates that these mosaic pyrobitumens contain more amorphous carbon related to other high molecular weight hydrocarbons in the tar mat and have a lower degree of order in their arrangement of aromatic layers. Overall, the precursor of the FM-F and FM-MM-F pyrobitumens from the PT1 well may be a tar mat enriched with QI and other high molecular weight hydrocarbons. QI inhibits the evolution of mosaic pyrobitumen to fibrous pyrobitumen.

5.2.3. *Hydrothermal temperature and optical texture of pyrobitumen*

The results of NMR and XRD show that the reservoir pyrobitumen has undergone substantial thermal evolution during its geological history. Based on thermal cracking and condensation reactions, fused-ring aromatic hydrocarbon molecules have formed inside the pyrobitumen, which has a relatively high thermal stability. It is an important reason why the asphaltic sample did not crack from 300 to 600 °C (Fig. 9). CH_4 was an important by-product resulting from pyrobitumen pyrolysis and polycondensation (Fig. 10); thus, the appearance of CH_4 represents the beginning of the internal pyrolysis and polycondensation reactions in pyrobitumen. There are apparent differences in the cracking and polycondensation temperatures among the pyrobitumen samples with various optical textures, representing the difference in the thermal stabilities of pyrobitumens with various optical textures. The pyrolysis

temperature of isotropic pyrobitumen was the lowest, while the pyrolysis temperature of fibrous pyrobitumen was the highest (Fig. 13). The pyrolysis temperature of FM-F pyrobitumen was the same as the alternating fibrous pyrobitumen (Fig. 13). The pyrolysis temperature of mosaic pyrobitumen ranged between those of fibrous and isotropic pyrobitumen (Fig. 13). For the mosaic pyrobitumen, FM and MM pyrobitumens had similar pyrolysis temperatures, while the pyrolysis temperature of MM-CM pyrobitumen was higher (Fig. 13).

Studies have shown that the temperature at which the pyrolysis and polycondensation reactions occur are related to the heating temperature experienced by the pyrobitumen (Yu et al., 2016; Chen, 2018; Fan, 2019). The higher the heating temperature the pyrobitumen is subjected to, the stronger is its thermal stability, and the higher the temperature at which the pyrolysis and polycondensation reaction occurs (Chen, 2018). Although the beginning temperature of the internal pyrolysis and polycondensation reaction of the pyrobitumen cannot represent the exact heating temperature, it can reflect the heating temperature (Chen, 2018). The existence of isotropic pyrobitumen represents the lowest hydrothermal temperature, while that of the fibrous pyrobitumen represents the highest, and that of the mosaic pyrobitumen is intermediate between the two. The FM-F pyrobitumen has undergone the same geological process as the alternated fibrous pyrobitumen and exhibits the same hydrothermal temperature (Fig. 13), confirming the validity of the experimental data. Overall, except for the QI-enriched pyrobitumen emplaced in the high-porosity section, when the optical texture of the pyrobitumen changes from isotropic→ FM → MM → CM → fibrous, the hydrothermal temperature gradually increases.

The QI-enriched pyrobitumen was primarily derived owing to the tar mat from the precipitation of heavy components in the crude oil. Although it had the same thermal history as the fibrous pyrobitumen, the high concentration of QI inhibited the fusion of mesophase spheres, forming only mosaic pyrobitumen (Figs. 12, 14). Except for the QI-enriched mosaic pyrobitumen, the isotropic, FM, MM, CM, and fibrous pyrobitumens have a good correlation between their H/C ratios and carbon interlayer spacings (Fig. 14). Specifically, the isotropic pyrobitumen has the highest H/C ratio and largest carbon interlayer spacing. As the optical textures of the pyrobitumen change from FM → MM → CM → fibrous, the H/C ratio and carbon interlayer spacing gradually decrease. This demonstrates that as the degree of polycondensation of the pyrobitumen increases, the degree of crystallinity and graphitization also gradually increase (Fig. 14). Furthermore, with the occurrence of reactions like dehydrogenation, bond breaking, polymerization and the escape of light components, the carbon concentration gradually increases, the hydrogen concentration gradually decreases, and H/C ratio gradually decreases. For the microcrystals in the pyrobitumen, the carbon interlayer spacing gradually decreases (White and Price, 1974; Stasiuk, 1997; Li et al., 2005). The optical textures of these reservoir pyrobitumen represent the internal molecular structure, resulting from the "heating treatment" of hydrothermal fluids. The different optical textures represent the differences in hydrothermal temperature. With the optical texture changes from isotropic → FM → MM → CM → fibrous, the hydrothermal fluid temperature gradually increases (Fig. 14).

Pyrobitumen with a tar mat precursor is enriched in QI and other high molecular weight hydrocarbons, forming only the mosaic structure. This type of pyrobitumen is concentrated in the high-porosity section of the reservoir (Fig. 12), not distributed on a large scale, and easy to identify. In addition, the optical texture of the reservoir pyrobitumen is closely related to the temperature of the hydrothermal fluid invading the reservoir, which can be used to characterize the hydrothermal temperature experienced by the reservoir.

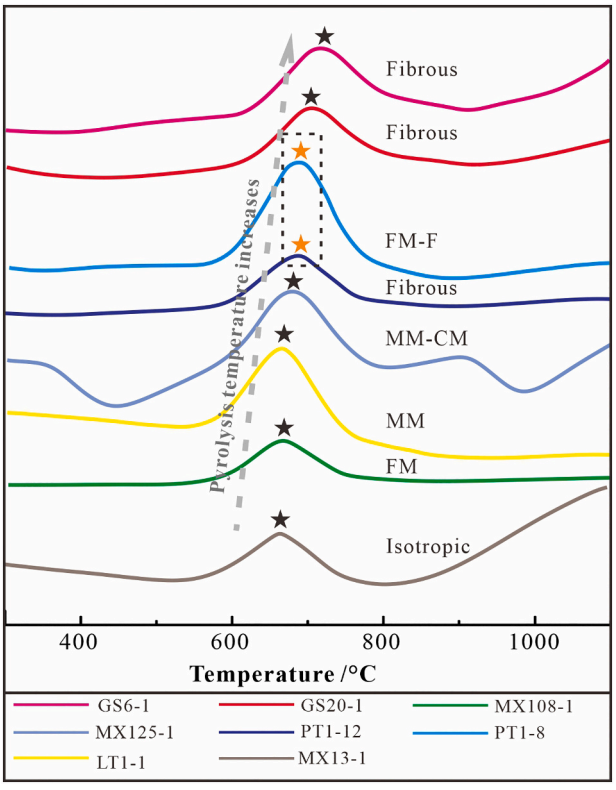

Fig. 13. Pyrolysis temperatures of the pyrobitumen with different optical textures during heating.
The pyrolysis temperatures of the isotropic, FM, MM, MM-CM, and fibrous pyrobitumens are 663, 670, 670, 680, and 700–716 °C, respectively. The FM-F pyrobitumen shows the same pyrolysis temperature as the alternately developed fibrous pyrobitumen (700 °C).

5.3. Hydrothermal activity

Pyrobitumens in the D-2 and D-4 members and LWM Formation are primarily anisotropic pyrobitumen with minor amounts of isotropic pyrobitumen. The isotropic pyrobitumen with a formation temperature of lower than 300 °C was not affected by the hydrothermal fluid. In addition, optically anisotropic pyrobitumen is widely developed in the DY and LWM Formation reservoirs, indicating that most of the DY and LWM Formation reservoirs had been transformed by hydrothermal activity.

For D-2, the fibrous pyrobitumen is widely observed in the Moxi and Gaoshiti areas, indicating high hydrothermal temperature. In addition, the pyrobitumen in the eastern area of Moxi gradually transforms into CM and MM pyrobitumens, indicating a weaker hydrothermal temperature (Fig. 15c). The hydrothermal temperature in D-4 was weaker than D-2, as the fibrous pyrobitumen in D-4 only develops in the southern region of Gaoshiti. The CM pyrobitumen are observed along the edge of the Deyang-Anyue Rift Trough and gradually transform into MM and FM pyrobitumens toward the northeast, indicating reduced hydrothermal temperature (Fig. 15b). The hydrothermal temperature in the LWM Formation is the weakest, as the fibrous pyrobitumen is only observed near well GS10 in the Gaoshiti area and gradually transforms into the CM and MM pyrobitumen to the northeast, indicating weaker hydrothermal temperature (Fig. 15d). Although there are significant differences in hydrothermal temperature in the three layers, the hydrothermal temperature change is the same, characterized by the strongest hydrothermal temperature in the Gaoshiti area and gradually weakening to the northeast.

Overall, the hydrothermal fluid may invade from great depths in the Gaoshiti area. As the hydrothermal fluid migrated vertically to the D-2 Member→ D-4 Member→ LMW Formation, the hydrothermal temperature gradually decreased, resulting in decreasing temperature characteristics in each layer from bottom to top (Fig. 15a). After the hydrothermal fluid invaded the DY and LWM Formation reservoirs from the Gaositi area, it migrated laterally toward the Moxi structure and

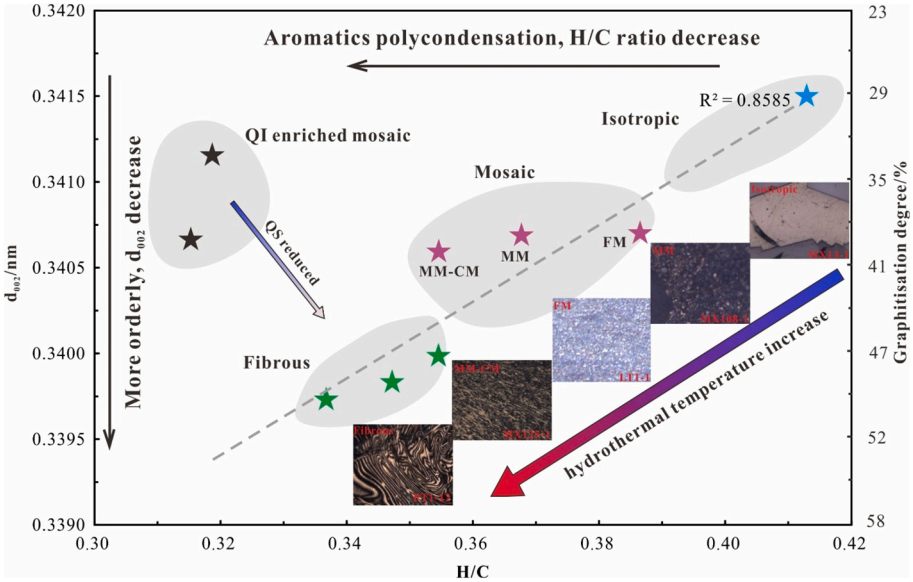

Fig. 14. Correlation diagram of optical texture, carbon layer spacing (d_{002}), and H/C ratio of the pyrobitumen in the DY and LWM reservoirs.
With the exception of a small amount of pyrobitumen whose precursor was QI-enriched tar mat, the H/C ratios of isotropic, FM, FM-MM and fibrous pyrobitumen have a good correlation with d_{002} and graphitization degree.

further east. During the lateral migration, the hydrothermal temperature gradually decreased (Fig. 15a).

5.4. Geological significance

The Emeishan mantle plume was active at the end of the Permian (262–251 Ma) (He, 2016). The results of in-situ U—Pb dating of saddle-shaped dolomite show that the invasion of hydrothermal fluid in the DY and LWM formations occured around 259.4 Ma (Su et al., 2020; Shen et al., 2019), which coincided with the time of the Emeishan mantle plume activity. Hydrothermal fluids invading the reservoirs had high temperature (>340 °C) and high salinity, suggesting that the hydrothermal fluid invading in the DY and LWM Formation reservoirs was related to the Emeishan mantle plume.

Studies on the hydrocarbon accumulation history in the central Sichuan Basin show that the charging time of the large-scale paleo-reservoir in the DY and LWM formations ranged from the end of the Permian to the Early Triassic, and crude oil cracking turned the paleo-oil reservoirs into gas reservoirs following the early Jurassic (Zheng et al., 2014; Wei et al., 2015a; Luo et al., 2015a, 2015b, 2015c; Shen et al., 2019; Su et al., 2020; Shen et al., 2021). When the hydrothermal fluid invaded the reservoirs, the paleo-temperature in the DY Formation established by burial history was only approximately120 °C, which was far from the temperature (>160 °C) for the large-scale cracking of crude oil. Nevertheless, a large number of pyrobitumens in the reservoirs formed during hydrothermal activity and had polycondensed into high-mature anisotropic pyrobitumen. Many natural gas inclusions composed of CH_4 are found in saddle dolomite, quartz, and other hydrothermal minerals, indicating that the crude oil in the paleo-oil reservoir had begun to crack when the high-temperature hydrothermal fluid invaded. This study found that, under this heating, the crude oil in the paleo-oil reservoirs had already cracked by the end of the Permian, advancing the predicted cracking time by approximately 60 Ma.

The spatial difference in hydrothermal temperature inevitably resulted in that of the crude oil cracking in the paleo-oil reservoir. The oil cracking caused by hydrothermal activity was strongest in the Gaoshiti area and gradually weakened laterally toward the northeast. Vertically, the oil cracking caused by the hydrothermal activity of D-2 was the strongest and gradually weakened in the D-4 Member and LWM Formation. The study on hydrothermal influence on the natural gas accumulation in the DY and LWM formations is of great significance for determining the natural gas accumulation and evolution process in the central Sichuan Basin. Our results provide a novel method for reconstructing the evolution process of ultra-deep gas reservoirs.

6. Conclusions

Using reflected-light microscopy, this study classified reservoir pyrobitumen in the Ediacaran-Low Cambrian strata. By integrating organic elements, carbon isotopes, NMR, XRD, TG-mass spectrometry, and fluid inclusion geochemistry, this study established the relationship between the pyrobitumen optical texture and the hydrothermal temperature, and discussed the influence of hydrothermal activity to crude oil cracking. The following conclusions can be drawn:

(1) There is a relationship between the optical structure of the pyrobitumen and hydrothermal temperature. With the exception of the QI-enriched pyrobitumen with a potential tar pad precursor, the optical texture of pyrobitumen changes from isotropic → FM → MM → CM → fibrous with increased hydrothermal temperature.
(2) Hydrothermal activity may be related to a mantle plume. The hydrothermal fluid may have invaded the strata of the D-2 and D-4 members and the LWM Formation along deep faults in the Gaoshiti area and migrated laterally to the northeast. The hydrothermal activity promoted the cracking of crude oil in the Ediacaran-Lower Cambrian reservoirs, which advanced the previously established cracking time of crude oil by approximately 60 Ma.
(3) Reservoir pyrobitumen can be used as a good indicator for hydrothermal activity in petroliferous basins. At the same time, in the exploration of deep natural gas reservoirs, attention should be paid to the influence of hydrothermal activity on natural gas accumulation history.

Author contributions

The manuscript was written through the contributions of all authors. All authors have given approval to the final version of the manuscript.

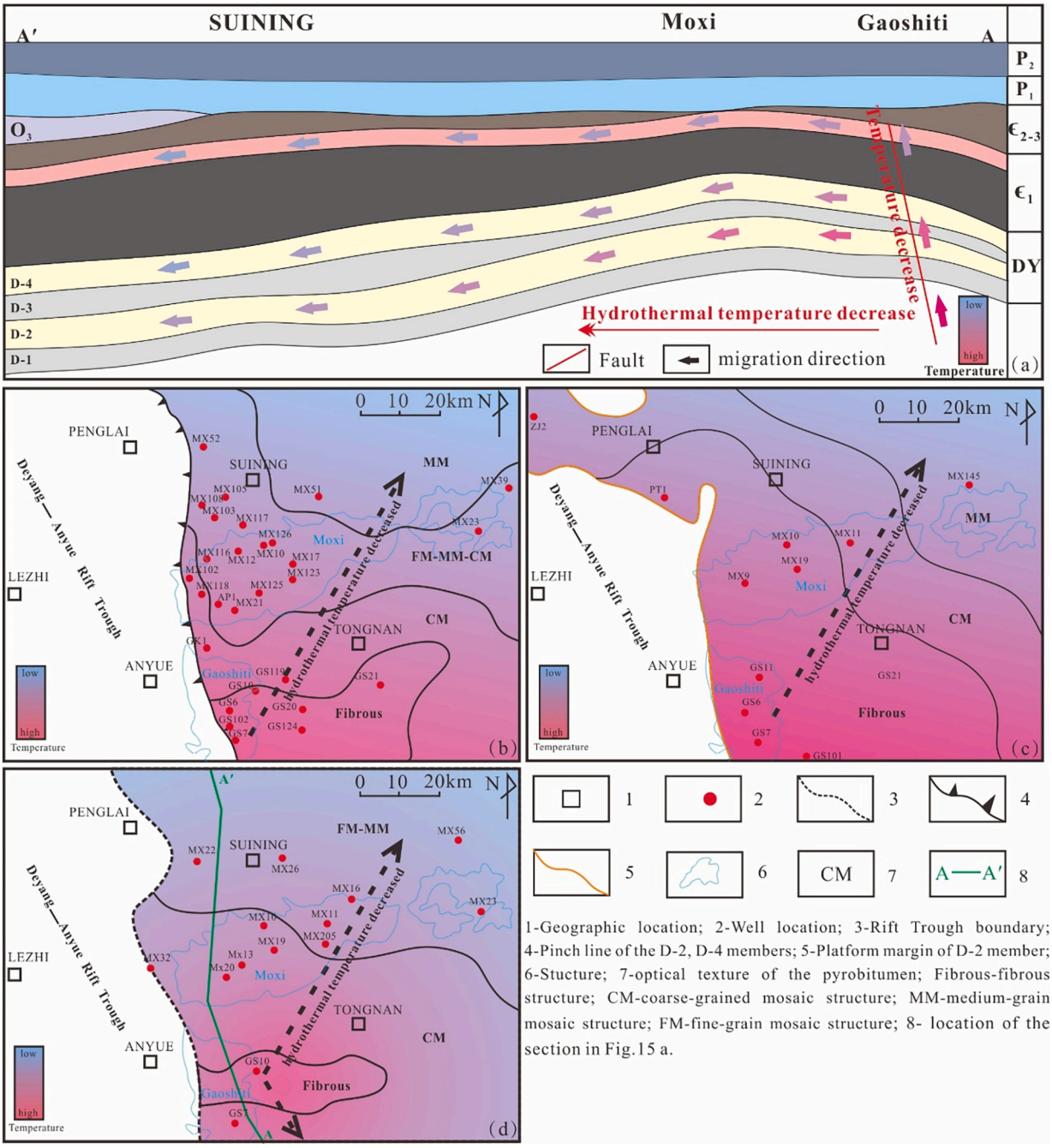

Fig. 15. Hydrothermal temperature diagrams in the DY and LWM formations. (a) Sectional view of hydrothermal transport direction; (b), (c) and (d) plane view of hydrothermal temperature distribution in the D-4 Member, D-2 Member, and LWM Formation, respectively.

Declaration of Competing Interest

The authors declare no competing financial interest.

Acknowledgements

This study was financially supported by the National Key R&D Program of China (Grant NO. 2017YFC0603106), the Youth Program of the National Natural Science Foundation of China (Grant NO.41802148). We would also thank the Exploration and Development Research Institute of the Southwest Oil and Gas Field Company PetroChina for providing core samples and necessary data.

References

Alvaraz, P., Sutil, J., Santamaria, R., 2008. Mesophase from anthracene oil-based pitches. Energy Fuel 22, 4146–4150.
Ban, L.L., Hess, W.M., 1971. A high-resolution electron microscopy study. In: Summary of Papers for 10th Biennial conference on Carbon, pp. 98–99.
Ban, L.L., Hess, W.M., 1976. Microstructure and morphology of carbon blacks. In: Petroleum Derived Carbons, ACS Symposium Series, 21, pp. 358–377.
Bouhadda, Y., Bormann, D., Sheu, E., 2007. Characterisation of Algerian Hassi-Messaoud asphaltene structure using Raman spectrometry and X-ray diffraction. Fuel. 86, 1855–1864.
Boven, A., Pasteels, P., Punzalan, L.E., Liu, J., Luo, X., Zhang, W., Guo, Z., Hertogen, J., 2002. 40Ar/39Ar geochronological constraints on the age and evolution of the Permo-Triassic Emeishan Volcanic Province, Southwest China. J. Asian Earth Sci. 20, 157–175.
Brooks, J.D., Taylor, G.H., 1965. Formation of graphitising carbons from the liquid phase. Nature. 3, 697–699.

Cai, C., Zhang, C., He, H., 2013. Carbon isotope fractionation during methane-dominated TSR in East Sichuan Basin gasfields, China: a review. Mar. Pet. Geol. 2013 (48), 100–110.
Chen, L., 2018. The Formation, Microstructure and Defects of Mesophase Pitch Based Carbon Materials. Hunan University.
Chen, X., Zhao, W.Z., Zhang, L.P., Zhao, Z.J., Liu, Y.H., 2012. Discovery and exploration significance of structure-controlled hydrothermal dolomites in the Middle Permian of the Central Sichuan Basin. Acta Pet. Sin. 33 (04), 562–569.
Cheng, X.L., Wang, B.C., 2009. The effect of carbonisation conditions on the structure of needle coke. Coal Convers. 32, 52–54.
Connan, J., Lacrampe-Couloume, G., Magot, M., 1995. Origin of gases in reservoirs[C]. In: Dolec D A. Proceedings of the 1995 International Gas Research Conference. Cannes: International Gas Union, 1996, pp. 21–61.
Du, J.H., Zou, C.N., Xu, C.C., He, H.Q., Shen, P., Yang, Y.M., Li, Y.L., Wei, G.Q., Wang, Z. C., Yang, Y., 2014. Strategic discovery and theoretical technology innovation of the Longwangmiao Formation extra-large gas field in the Central Sichuan paleo-uplift. Pet. Explor. Dev. 41, 268–277.
Du, J.H., Zhang, B.M., Wang, Z.C., Zou, C.N., Xu, C.C., Shen, P., Zhang, J., Zhang, J., Zhou, H., Jiang, H., Wen, L., Shan, X.Q., Liu, J.J., 2016. The carbonate gentle slope of the lower Cambrian Longwangmiao Formation in the Sichuan Basin Sedimentary model and reservoir genesis of grain beach. Nat. Gas Ind. 36, 1–10.
Eksilioglu, A., Gencay, N., Yardim, M.F., 2006. Mesophase AR pitch derived carbon foam: effect of temperature, pressure and pressure release time. J. Mater. Sci. 41, 2743–2748.
Fan, X.H., 2019. Study on Large Polycyclic Aromatic Hydrocarbons in Coal Tar Pitch and its Extracted Fractionations and Thermal Condensations. Hunan University.
Fanjul, M., Granda, M., Santamaria, R., 2003. Pyrolysis behavior of stabilised self-sintering mesophase. Carbon. 41, 413–422.
Fathollahi, B., Jones, B., Chau, P.C., 2005. Injection and stabilisation of mesophase pitch in the fabrication of carbon-carbon composites. Part III: Mesophase stabilisation at low temperatures and elevated oxidation pressures. Carbon. 2005 (43), 143–151.
Feng, M.Y., Wu, P.C., Qiang, Z.T., Liu, X.H., Duan, Y., Xia, M.L., 2017. Hydrothermal dolomite reservoir in the Precambrian Dengying Formation of Central Sichuan Basin, Southwestern China. Mar. Pet. Geol. 82, 206–219.
Feng, Q.F., Xiao, Y.X., Hou, X.L., Chen, H.K., Wang, Z.C., Feng, Z., 2021. Logging identification method of depositional facies in Sinian Dengying Formation of the Sichuan Basin. Pet. Sci. 18 (04), 1086–1096.
Figueiras, A., Granda, M., Casal, E., 1998. Influence of primary QI on Pitch Pyrolysis with reference to unidirectional C/C composites. Carbon. 36, 883–891.
Forrest, M., Marsh, H., 1981. Composition of pore-wall material in metal-lurgical coke: considerations of strength, gasification and thermal stress. Fuel. 60, 418–422.
Gao, P., Liu, G.D., Wang, Z.C., Jia, C.Z., Wang, T.S., Zhang, R.W., 2017. Rare earth dements (REEs) geochemistry of Sinian-Cambrian reservoir solid bitumens in Sichuan Basin, SW China: potential application to petroleum exploration. Geol. J. 52, 298–316.
Gao, P., Liu, G.D., Lash, G.G., Li, B.Y., Yan, D.T., Chen, C., 2018. Occurrences and origin of reservoir solid bitumen in Sinian Dengying Formation dolomites of the Sichuan Basin, SW China. Int. J. Coal Geol. 200, 135–152.
Gize, A.P., 1986. The development of a thermal mesophase in bitumens from high temperature ore deposits[C]. In: Dean W E. Organics and Ore Deposits. Denver Region Exploration Geologists' Society, Wheat Ridge, pp. 137–150.
Gong, Q.M., Huang, Q.Z., Huang, B.Y., 2001. Mesophase formation of coal-tar Pitches used for impregnant of C/C composites. Trans. Nonferrous Metals Soc. China (English Edition). 11, 483–487.
Goodarzi, F., 1985. Optical properties of vitrinite carbonized under pressure. Fuel 64, 158–162.
Goodarzi, F., 1993. Optical characteristics of heat-affected bitumens from the Nanisivik Mine, N.W. Baffin Island. Arctic Canada. Energy Sources. 15, 359–376.
Goodarzi, F., Stasiuk, L.D., 1991. Thermal alteration of gilsonite due to bushfire, an example from Southwest Iran. Int. J. Coal Geol. 17 (3–4), 333–342.
Grint, A., Swietlik, U., Marsh, H., 1979. Carbonisation and liquid-crystal (mesophase) development. The co-carbonisation of vitrains with Ashland A200 petroleum pitch. Fuel. 58, 642–650.
Hatshorme, N.H., 1974. The Microscopy of Liquid Crystals, Monographs in Microscopic Series. Microscope Publications, London.
He, B.H., 2016. Research status on some issues of the Emeishan Great Igneous Rock Province. Adv. Earth Science 31 (01), 23–42.
He, B., Xu, Y.G., Xiao, L., Wang, K.M., Sha, S.L., 2003. The formation mechanism and spatial distribution of the Emeishan large igneous province: new evidence from sedimentary stratigraphy. Acta Geol. Sin. 02, 194–202.
Heidenreich, R.D., Hess, W.M., Ban, L.L., 1968. A test object and criteria for high resolution electron microsopy. J. Appl. Crystallogr. 1, 1–19.
Holman, A.I., Grice, K., Jaraula, C.M.B., Schimmelmann, A., 2014. Bitumen II from the Paleoproterozoic Here's Your Chance Pb/Zn/Ag deposit: Implications for the analysis of depositional environment and thermal maturity of hydrothermally-altered sediments. Geochim. Cosmochim. Acta 139, 98–109.
Hu, Y.J., Cai, C.F., Pederson, C.L., Liu, D.W., Jiang, L., 2020. Dolomitization history and porosity evolution of a giant, deeply buried Ediacaran gas field (Sichuan Basin, China). Precambrian Res. 338, 105595.
Huang, K.N., Opdyke, N.D., 1998. Magnetostratigraphic investigations on an Emeishan basalt section in western Guizhou province, China. Earth Planet. Sci. Lett. 163 (1–4), 1–14.
Hunt, J.M., 1996. Petjoleum Geology and Geochemistry, Seconded. Freeman and Company, New York, pp. 1–743.
Inoue, A., 1995. Formation of clay minerals in hydrothermal environments. In: Velde B. Origin and Mineralogy of Clays. Berlin: Spring, pp. 268–329.
Jacob, H., 1989. Classification, structure, genesis and practical importance of natural solid oil bitumen ("migrabitumen"). Int. J. Coal Geol. 11, 65–79.
Jiang, Y.Q., Tao, Y.Z., Gu, Y.F., Wang, J.B., Qiang, Z.Q., 2016a. Hydrothermal dolomitization in Sinian Dengying Formation, Gaoshiti-Moxi area, Sichuan Basin, SW China. Pet. Explor. Dev. 43 (01), 51–60.
Jiang, Y.Q., Tao, Y.Z., Gu, Y.F., Wang, J.B., Qiang, Z.T., Jiang, N., Lin, G., Jiang, C., 2016b. Hydrothermal dolomitisation of Dengying Formation in Gaoshiti-Moxi area, Sichuan Basin. Pet. Explor. Dev. 43 (01), 51–60.
Jiang, Y.Q., Gu, Y.F., Li, K.H., Li, S., Luo, M.S., He, B., 2018a. The types and genesis of storage and seepage space of Middle Permian hydrothermal dolomite in the Central Sichuan Basin. Nat. Gas Ind. 38 (02), 16–24.
Jiang, Y.Q., Gu, Y.F., Li, K.H., Li, S., Luo, M.S., He, B., 2018b. Space types and origins of hydrothermal dolomite reservoirs in the Middle Permian strata, Central Sichuan Basin. Nat. Gas Ind. 38 (02), 16–24.
Jiang, Y.Q., Gu, Y.F., Zhu, Y.F., 2019. Carbonate Hydrothermal Transformation Activities. Science Press.
Jin, M.D., Tan, X.C., Zeng, W., Li, L., Li, Z.Y., Luo, B., 2016. Reconstruction of the tectonic paleogeomorphology of Longwangmiao Formation during the Caledonian-Hercynian period in Moxi-Gaoshiti area. Sichuan Basin Geol. Significance. 34 (04), 634–644.
Khavari-Khorosani, G., Murchison, D.G., 1978. Thermally metamorphosed bitumen from Windy Knoll, Derbyshire, England. Chem. Geol. 22, 91–105.
Landis, C.R., Castaño, J.R., 1995. Maturation and bulk chemical properties of a suite of solid hydrocarbons. Org. Geochem. 22, 137–149.
Lewis, I.C., 1987. The chemistry of pitch carbonization. Fuel. 66 (11), 1527–1533.
Li, X., Li, Q., 1996. Rheological properties and carbonisation of coal-tar pitch. Fuel. 75, 3–7.
Li, T.Q., Wang, C.Y., 2005. Study on the formation mechanism of carbonaceous mesophase. New Carbon Mater. 20, 278–285.
Li, T.Q., Wang, C.Y., Liu, X.J., 2005. Characteristics of mesocarbon microbeads generated from a coal tar pitch with addition of micro-alumina powder. Fuel Process. Technol. 87, 77–83.
Lin, X.M., Yuan, H.F., Zhu, L.Q., Zeng, W., Xu, Y.Q., 2020. Hydrocarbon accumulation history of the Cambrian Longwangmiao Formation in the Anyue structure of the Central Sichuan basin. Acta Geol. Sin. 94 (03), 916–930.
Liu, W., 2018. Study on Pore Pressure of the Sinian-Paleozoic in the Central and Western Sichuan Basin. China University of Petroleum, Beijing.
Liu, Y.H., Luo, Y.H., Cheng, J., 2003a. Research on the preparation of needle coke from petroleum residue. New Carbon Mater. 18, 128–132.
Liu, X.J., Wang, C.Y., Li, T.Q., 2003b. The effect of phenolic resin on the formation of homogeneous nucleated mesophase carbon microspheres. Carbon Technol. 124, 1–4.
Luo, B., Luo, W.J., Wang, W.Z., 2015a. The formation mechanism of Sinian gas reservoirs in Leshan-Longnüsi paleo-uplift, Sichuan Basin. Nat. Gas Geosci. 26 (03), 444–455.
Luo, B., Luo, W.J., Wang, W.Z., Wang, Z.H., Shan, S.J., 2015b. Formation mechanism of the Sinian natural gas reservoir in the Leshan-Longnvsi Paleo-uplift, Sichuan Basin. Nat. Gas Ceosci. 26, 2015.
Luo, B., Yang, Y.M., Luo, W.J., Wen, L., Wang, W.Z., Chen, K., 2015c. Reservoir development control factors and distribution of Dengying Formation in Central Sichuan paleo-uplift. Acta Pet. Sin. 36, 416–426.
Mankiewicz, P.J., Pottorf, R.J., Kozar, M.G., 2009. Gas geochemistry of the Mobile Bay Jurassic Norphlet Formation: thermal controls and implications for reservoir connectivity. AAPG Bull. 93 (10), 1319–1346.
Manzano, B.K., Fowler, M.G., Machel, H.G., 1997. The influence of thermochemical sulphate reduction on hydrocarbon composition in Nisku reservoirs, Brazeau river area, Alberta, Canada. Org. Geochem. 27 (7–8), 507–521.
Mao, J.D., Fang, X.W., Lan, Y.Q., Schimmelmann, A., Mastalerz, M., Xu, L., Schmidt-Rohr, K., 2010. Chemical and nanometer-scale structure of kerogen and its change during thermal maturation in vestigated by advanced solid-state 13C NMR spectroscopy. Geochim. Cosmochim. Acta 74, 2110–2127.
Marsh, H., 1973. Carbonization and liquid-crystal (mesophase) development: part 1. The significance of the mesophase during carbonisation of coking coals. Fuel. 52, 205–212.
Marsh, H., Cornford, C., 1976. Mesophase: The precursor to graphitisable carbon. In: Deviney, M.L., O'Grady, T.M. (Eds.), Petroleum Derived Carbons, 21. American Chemical Society, pp. 266–281.
Mochida, I., Ando, T., Maeda, K., 1980. Catalytic carbonisation of aromatic hydrocarbons-IX: Carbonisation mechanism of heterocyclic sulfur compounds leading to the anisotropic coke. Carbon. 18, 131–136.
Pang, X.Q., 2010. Key challenges and research methods of petroleum exploration in the deep of superimposed basins in western China. Oil Gas Geol. 31, 517–541.
Patrick, J.W., Reynolds, M.J., Shaw, F.H., 1973. Development of optical anisotropy in vitrains during carbonisation. Fuel. 52, 198–204.
Qian, S., Li, C.F., Zhou, G.Y., 1984. The relationship between the composition structure of carbonised raw materials and the mesophase structure. J. Fuel Chem. Technol. 12, 348–360.
Rimmer, S.M., Crelling, J.C., Yoksoulian, L.E., 2015. An occurrence of coked bitumen, Raton Formation, Purgatoire River Valley, Colorado, U.S.A. Int. J. Coal Geol. 141-142, 63–73.
Sanada, Y., 1978. Utilisation of heavy oil carbonisation and carbon materials. J. Fuel Soc. Japan. 57, 117–131.
Shan, X.Q., Zhang, J., Zhang, B.M., Liu, J.J., Zhou, H., Wang, Y.J., Fu, Z.W., 2016. Characteristics of dolomite karst reservoirs in the Sinian Dengying Formation in the Sichuan Basin and evidence of dissolution. Acta Pet. Sin. 37, 17–29.
Shen, Z.M., 2003. New Carbon Materials. Chemical Industry Press, Beijing.

Shen, A.J., Hu, A.P., Cheng, T., Liang, F., Pan, W.Q., Feng, Y.X., Zhao, J.X., 2019. Laser in-situ U-Pb isotope dating technology and its application in carbonate diagenesis and pore evolution. Pet. Explor. Dev. 46, 1062–1074.
Shen, A.J., Zhao, W.Z., Hu, A.P., Wang, H., Liang, F., Wang, Y.S., 2021. Carbonate mineral dating and temperature fixation technology and its application in the study of oil and gas accumulation in the Central Sichuan paleo-uplift. Pet. Explor. Dev. 48, 476–487.
Shi, C.H., Cao, J., Tan, X.C., Luo, B., Zeng, W., Hu, W.X., 2017. Discovery of oil bitumen co-existing with solid bitumen in the Lower Cambrian Longwangmiao giant gas reservoir,Sichuan Basin, southwestern China: implications for hydrocarbon accumulation process. Org. Geochem. 108, 61–81.
Song, H.H., 1996. Research on Reaction Design of High-Quality Mesophase Synthesis and Preparation of High-Performance Pitch-Based Carbon fiber. Shanxi Institute of Coal Chemistry, Chinese Academy of Sciences.
Song, Z.Z., Liu, G.D., Luo, B., Zeng, Q.C., Tian, X.W., Dai, X., Jiang, R., 2021. Logging evaluation of solid bitumen in tight carbonate in deep-buried and ultra-deep-buried srtrata of the Central Sichuan basin. Acta Sedimentol. Sin. 39 (01), 197–211.
Stasiuk, L.D., 1997. The origin of pyrobitumens in upper Devonian Leduc formation gas reservoirs, Alberta, Canada: an optical and EDS study of oil to gas transformation. Mar. Pet. Geol. 14, 915–929.
Su, A., Chen, H.H., Feng, Y.X., Zhao, J.X., Nguyen, A.D., Wang, Z.C., Long, X.P., 2020. Dating and characterising primary gas accumulation in Precambrian dolomite reservoirs, Central Sichuan Basin, China: Insights from pyrobitumen Re-Os and dolomite U-Pb geochronology. Precambrian Res. 350, 105897.
Sun, L.D., Zou, C.N., Zhu, R.K., 2013. Formation, distribution and potential of deep hydrocarbon resources in China. Pet. Explor. Dev. 40, 641–649.
Sun, S.H., Yu, H., Xu, Y.L., Wu, L., Zhu, Y.M., Zhao, X.F., 2020. Preparation and characterisation of high softening point coated asphalt. Appl. Chem. Indust. 49, 2437–2441.
Tao, Z., Xu, B., 1987. Research on the pyrolysis process of coal pitch using differential thermal and thermogravimetric analysis. Carbon. 1, 34–41.
Taylor, G.H., 1961. Development of optical properties of coke during carbonisation. Fuel. 40, 465–472.
Taylor, G.H., Pennock, G.M., Fitz Gerald, J.D., 1993. Influence of QI on mesophase structure. Carbon. 31, 341–354.
Tian, X.W., Hu, G.Y., Li, W., Li, X.Q., Su, G.P., Xu, Y.R., Cai, D., Wei, H.P., 2013. Geochemical characteristics and significance of Sinian reservoir asphalt in Leshan-Longnüsi paleo-uplift area, Sichuan Basin. Nat. Gas Geosci. 24 (05), 982–990.
Tian, X.W., Yang, D.L., Zhong, J.Y., Sun, Y.T., Wang, Y.L., Yang, Y., 2021. Microscopic characterization of dolomite reservoirs by CT imaging: a case study of the Dengsi Formation in Moxi-Longnvsi area, Central Sichuan. Acta Sedimentol. Sin. 39 (05), 1264–1274.
Tissot, B.P., Welte, D.H., 1984. Petroleum Formation and Occurrence. Spring-Verlag, Berlin, Heidelberg, New York, pp. 1–678.
Wang, Z.Y., Fan, P., Cheng, K.M., 1995. The thermal evolution indicator of carbonate rocks. Sci. China B. 733–740.
Wang, H.Y., Wang, B.C., Xu, B.S., 2008. Preparation and formation mechanism of mesocarbon microspheres under the action of a magnetic field. Coal Convers. 31, 67–70.
Wang, G.Z., Liu, S.G., Chen, C.H., Wang, D., Sun, W., 2013. The relationship between the Heba MVT lead-zinc deposit and paleo-oil and gas reservoirs in the southeastern margin of the Sichuan Basin. Earth Sci. Front. 20, 107–116.
Waples, D.W., 2000. The kinetics of in-reservoir oil destruction and gas formation: constraints from experimental and empirical data, and from thermodynamics. Org. Geochem. 31, 553–575.
Wei, G.Q., Xie, Z.Y., Song, J.R., Yang, W., Wang, Z.H., Li, J., Wang, D.L., Li, Z.S., Xie, W. R., 2015a. Sinian-Cambrian natural gas characteristics and genesis of the Central Sichuan paleo-uplift in the Sichuan Basin. Pet. Explor. Dev. 42, 702–711.
Wei, G.Q., Yang, W., Du, J.H., Xu, C.C., Zou, C.N., 2015b. Tectonic features of Gaoshiti-Moxi paleo-uplift and its controls on the formation of a giant gas field, Sichuan Basin, SW China. Pet. Explor. Dev. 42, 257–265.
Werner-Zwanziger, U., Lis, G., Mastalerz, M., Schimmelmann, A., 2005. Thermal maturity of type II kerogen from the New Albany Shale assessed by 13C CP/MAS NMR. Solid State Nucl. Magn. Reson. 38, 140–148.
White, J.L., 1976. Mesophase mechanisms in the formation of the microstructure of petroleum coke. In: Deviney, M.L., O'Grady, T.M. (Eds.), Petroleum Derived Carbons: American Chemical Society, pp. 282–314.
White, J.L., Price, R.J., 1974. The formation of mesophase microstructures during the pyrolysis of selected Coker feedstocks. Carbon. 12, 321–333.
Wilhelms, A., Larter, S.R., 1995. Overview of the geochemistry of tar mats North Sea and USA: implications for tar mat formation. In: Cubitt, J.M., England, W.A. (Eds.), The Geochemistry of Reservoirs, 86. Geological Society Special Publication, pp. 87–102.
Wilson, N.S.F., 2000. Organic petrology, chemical composition, and reflectance of yrobitumen from the El Soldado Cu deposit, Chile. Int. J. Coal Geol. 43, 53–82.
Wu, B.Y., 2006. Study on the Pyrolysis Condensation of Coal-Tar Pitch Used for Carbon Materials Manufacture. Wuhan University of Science and Technology.
Wu, Y., Zhang, C.Q., Mao, J.W., Zhang, W.S., Wei, C., 2013. Oil and gas organic matter and the mineralisation of MVT lead-zinc deposit: a case study of Chipu lead-zinc deposit in Sichuan. Acta Geosci. 34, 425–436.
Xie, Z.Y., Li, J., Yang, C.L., Tian, X.W., Zhang, L., 2021. Geochemical characteristics of Sinian-Cambrian natural gas in Central Sichuan paleo-uplift and exploration potential of Taihe gas area. Nat. Gas Ind. 41, 1–14.
Xu, F.H., 2017. Fluid System and Hydrocarbon Accumulation in the Sinian Dengying Formation and Cambrian Longwangmiao Formation in the Central Sichuan Basin. Chengdu University of Technology.
Xu, B., Li, T.H., Pan, L.H., 2002. Study on the effect of quinoline insolubles on thermal polymerisation modification of coal pitch. J. Fuel Chem. Technol. 30, 418–422.
Xu, C.C., Shen, P., Yang, Y.M., Luo, B., Huang, J.Z., Jiang, X.F., Xie, J.R., Cen, Y.J., 2014. The natural gas accumulation conditions and enrichment rules of the Sinian-lower Cambrian Longwangmiao Formation in the Leshan-Longnüsi paleo-uplift. Nat. Gas Ind. 34, 1–7.
Yamada, Y., Imamura, T., Kakiyama, H., 1974. Characteristics of meso-carbon microbeads separated from pitch. Carbon. 12, 307–319.
Yang, Y.S., 2011. Preparation of Mesophase Carbon Material and its Electrochemical Performance. Tianjin University.
Yang, C.Y., Ni, Z.Y., Li, M.J., 2018. Pyrobitumen in South China: Organic petrology, chemical composition and geological significance. Int. J. Coal Geol. 188, 56–63.
Yokono, T., Yamada, J., Sanada, Y., 1986. Formation of carbon microbeads from paraffin / pitch systems under mild pressure and temperature conditions. J. Mater. Sci. Lett. 5, 779–780.
Yu, F., Chen, L., Fei, Y.Q., 2016. Investigating carbonization of mesophase pitch fibers by thermo-gravimetric analysis. Min. Metal. Eng. 36 (4), 100–108.
Yuan, B., Mao, J.W., Yan, X.H., Wu, Y., Zhang, F., Zhao, L.L., 2014. The source and mechanism of mineralisation of the Daliangzi lead-zinc deposit: Sulfur, carbon, hydrogen, oxygen, strontium isotopes and the restriction of sphalerite trace elements. Acta Petrol. Sin. 30, 209–220.
Zhang, H.Q., 2007. Study on the Preparation of Ordered Mesophase Coke with Soft Pitch as Raw Material. Shanghai Normal University, Shanghai.
Zhang, P.Y., 2019. Study on the Genesis Mechanism of Hydrogen Sulfide in Sinian Cambrian Gas Reservoir in Central Sichuan Region. University of Petroleum of China (Beijing).
Zhang, C.Q., Li, X.H., Yu, J.J., Mao, J.W., Chen, F.K., Li, H.M., 2008. The rubidium-strontium dating and geological significance of sphalerite bed sheet particles in the Daliangzi lead-zinc mine, Sichuan. Geol. Rev. 04, 532–538.
Zhang, C.Q., Rui, Z.Y., Chen, Y.C., Wang, D.H., Chen, Z.H., Lou, D.B., 2013. Pb-zinc mineral resource potential and main strategic continuation areas in China. Chinese Geol. 40, 248–272.
Zheng, P., Shi, Y.Y., Zou, C.Y., Kong, L.M., Wang, L.S., Liu, J.Z., 2014. Analysis of natural gas source of Dengying Formation and Longwangmiao Formation in Gaoshiti-Moxi area. Nat. Gas Ind. 34, 50–54.
Zhong, Y.T., He, B., Mundil, R., 2014. CA-TIMS zircon U-Pb dating of felsic ignimbrite from the Binchuan section: Implications for the termination age of Emeishan Large Igneous Province. Lithos. 204 (3), 14–19.
Zhou, J.G., Xu, C.C., Yao, G.S., Yang, G., Zhang, J.Y., Hao, Y., Wang, F., Pan, L.Y., Gu, M. F., Li, W.Z., 2015. Formation and evolution of the lower Cambrian Longwangmiao Formation reservoir in the Sichuan Basin. Pet. Explor. Dev. 42, 158–166.
Zhou, J.G., Zhang, J.Y., Deng, H.Y., Chen, Y.N., Hao, Y., Li, W.Z., Gu, M.F., Luo, X.Y., 2017. Lithofacies paleogeography and sedimentary model of the Sinian Dengying Formation in Sichuan Basin. Nat. Gas Ind. 37, 24–31.
Zhu, G.Y., Wang, T.S., Xie, Z.Y., Xie, B.H., Liu, K.Y., 2015. Giant gas discovery in the Precambrian deeply buried reservoirs in the Sichuan Basin, China: implications for gas exploration in old cratonic basins. Precambrian Res. 262, 45–66.
Zhu, L.Q., Liu, G.D., Song, Z.Z., 2022. Reservoir solid bitumen-source rock correlation using the trace and rare earth elements–implications for identifying the natural gas source of the Ediacaran-lower Cambrian reservoirs, Central Sichuan Basin[J]. Mar. Pet. Geol. 137, 105499.
Zou, C.N., Wei, G.Q., Xu, C.C., Du, J.H., Xie, Z.Y., Wang, Z.C., Hou, L.H., Yang, C., Li, J., Yang, W., 2014. Geochemistry of the Sinian–Cambrian gas system in the Sichuan Basin, China. Org. Geochem. 74, 13–21.